Investigation of the Rotor-Obstacle Aerodynamic Interaction in Hovering Flight

D. Zagaglia
Post-Doc Research Fellow
Politecnico di Milano
Dipartimento di Scienze e Tecnologie Aerospaziali
Via La Masa 34, 20156 Milano, Italy
and
M. Giuni, D.J. Pickles, R.B Green
Aerospace Science Division
School of Engineering
University Of Glasgow
Glasgow
United Kingdom

Abstract

In this paper a comprehensive experimental survey of the aerodynamic interaction of a hovering rotor in the proximity of a ground obstacle is described, taking advantage of multiple experimental techniques. Load measurements on the rotor were carried out in order to assess the change in the rotor performance for different positions with respect to the cubic obstacle, thus simulating a set of possible hovering flight conditions around the obstacle. Laser Doppler Anemometry (LDA) measurements of the rotor inflow were used in order to investigate how the aerodynamic interaction affected the rotor performance. A flow visualisation survey was performed using a smoke wand and particle image velocimetry, and surface pressure measurements on the obstacle were taken. Two independent PIV experiments were performed. Stereoscopic Particle Image Velocimetry (SPIV) measurements in the region between the rotor and the obstacle were carried out in order to

have a better insight of the interacting flow field. PIV was also performed on a very small scale rotor and obstacle in a different facility.

NOMENCLATURE

A	Rotor disk area πR^2
c	Blade chord
C_p	Obstacle surface pressure coefficient $\frac{p-p_\infty}{0.5\rho V_{TIP}^2}$
c_Q	Rotor torque coefficient, $Q/(\rho V_{TIP}^2 AR)$
C_T	Rotor thrust coefficient $\frac{T}{\rho A V_{TIP}^2}$
D	Rotor diameter
F	Force on obstacle surface
FM	Figure of Merit, $C_T^{3/2}/(C_Q\sqrt{2})$
H	Rotor height above ground
M	PIV optical magnification factor
M_{TIP}	Mach number at Blade tip, V_{TIP}/c_∞
Q	Rotor torque
p	Obstacle surface pressure
p_∞	Ambient pressure
R	Rotor radius
Re_{TIP}	Reynolds number at Blade tip, $V_{TIP}c/\nu$
T	Rotor thrust
u	Velocity in the x (horizontal) direction
V_T	Rotor blade tip speed,ΩR
x,y,z	coordinate system on the obstacle face
(X, Y, Z)	Absolute reference System, Z also used for rotor height above ground, equivalent to H
X	Displacement between the rotor axis and the obstacle front face
v	Velocity in the vertical direction
Δt	Laser pulse delay time
ν	Fluid kinematic viscosity
ϵ_{c_T}	Uncertainty on the Thrust coefficient
ϵ_u	Uncertainty on the PIV velocity field, in-plane velocity components
$\epsilon_{u,op}$	Uncertainty on the PIV velocity field, out-of-plane velocity components
θ	Half camera separation angle
Ω	Rotational frequency of the rotor
ρ	Air density
Ω	Rotor rotational speed
CFD	Computational Fluid Dynamics
FFT	Fast Fourier Transform
IGE	In Ground Effect
OGE	Out Of Ground Effect
PIV	Particle Image Velocimetry
RMS	Root Mean Square
AG22	GARTEUR Action Group 22
CIRA	Centro Italiano Ricerche Aerospaziali, Italian Aerospace Centre
DI	Dynamic Interface
DLR	Deutsches Zentrum fur Luft- und Raumfahrt, German Aerospace Centre
GARTEUR	Group for Aeronautical Research and Technology in EURope
IHST	International Helicopter Safety Team

1 INTRODUCTION

The helicopter is a very versatile flying machine which is often required to operate within confined areas, owing to its ability to hover and fly under control at very low-speed . These challenging operations areas typically comprise naval environments, e.g. a landing manoeuvre on a helicopter carrier, and rescue operations in confined areas and urban environments where the helicopter interacts with the surrounding buildings.

The aerodynamic interaction between the rotor-induced wake and surrounding obstacles, such as buildings and mountain walls, typically generates, on the one hand, a degradation of the helicopter performance and high compensatory workload for the pilot (Ref.[4]), on the other hand unsteady forces which can stress the structure of the surrounding obstacles. The danger intrinsic to these flight conditions is evident in the accident database of Ref.[11], collected by the Joint Helicopter Safety Analysis Team (JHSAT) for the International Helicopter Safety Team (IHST). The gathered database analyses 523 helicopter accidents that occurred in the United States of America in 2000, 2001 and 2006, sorting them in terms of flight phase, occurrence category and motivation. This study highlighted that most of the helicopter accidents (61.4 %) occur during take-off and landing, hence potentially in the presence of ground obstacles. In particular, 41% of the total number of accidents were attributed to pilot performance management issues, i.e. the fact that the pilot was not capable of accounting for the change in the helicopter performance due to external perturbations.

The number of experimental studies regarding the rotor interaction with simplified geometries (i.e. semi-infinite vertical walls, parallelepipeds, etc.) is unexpectedly small in comparison to those comprising more complex geometries (e.g. ship superstructures). Among these, Timm in Ref.[10] was the first to observe the flow recirculation induced by the interaction between the rotor and obstacle through flow visualisation. Iboshi et al. investigated in Ref.[2] the ground effect of a fully articulated rotor in ground effect above a confined area between two vertical walls, finding that the re-circulatory flow upward along the wall causes both the steady and vibratory torque coefficients to increase. The effect is either a downwash or up-wash based on the combinations of the wall height, the space between walls, and the rotor height.

For the helicopter interaction with more complex geometries, the Dynamic Interface problem (Ref.[13]), i.e. the launch and recovery of flight vehicles, primarily rotorcraft, onto ships, is probably the most investigated configuration from both the experimental and numerical point of view. On this topic, one of the

first experimental works was produced by Zan in Ref.[12], where he presented the experimental measurements of time-averaged rotor thrust coefficients for a rotor immersed in the airwake of the Canadian Patrol Frigate ship. Further studies allowed to investigate also the unsteady loads on the fuselage immersed in the ship wake (Lee and Zan, Ref.[5]) and the full configuration comprising rotor and fuselage (Lee and Zan Ref.[6]). The experimental investigations found in the literature do not only focus on the change in the rotor performance, but they also rely on other kind of flow measurements. As an example, Quinliven at al. (Ref.[8]) investigated the inflow region and the wake of a rotor in proximity of a building model, highlighting the effect of the flow-recirculation that occurs when the rotor is close to the building. A different measurement technique was adopted by Rajagopalan et al in Ref.[9], where Particle Image Velocimetry (PIV) was used to acquire 3-component velocity field measurements of the combined wake of a tandem-rotor helicopter and a ship. PIV was also used by Konuş and Savaş in Ref.[3] to investigate the rotor wake in close proximity to vertical walls, and by Nacakli and Landman in Ref.[7] to investigate the recirculation region between a rotor and the vertical wall of a ship deck.

Despite the presence of several numerical and experimental works, a systematic study of these aerodynamic phenomena is lacking. The GARTEUR Action Group 22 *"Forces on Obstacles in Rotor Wake"*, comprising several universities (Politecnico di Milano, University of Glasgow, National Technical university of Athens) and research institutes (CIRA, DLR, ONERA, NLR), originates from the idea of promoting activities which could contribute to a better understanding of these phenomena. In this framework, the production of an experimental database was carried out initially at Politecnico di Milano (Ref.[1]), analysing the case of a model helicopter with fuselage interacting with a cuboid obstacle. Following this first experience, an extended database comprising several measurement points and experimental techniques was produced at University of Glasgow with a deeper insight on the interacting flow, which is the subject of the present paper.

As previously stated a systematic study of the aerodynamic phenomena involved is still lacking. Moreover the past investigations usually either rely on just one measurement technique or they usually involve quite specific geometries (e.g. ships). The idea behind the present work is thus to experimentally investigate this problem, simplifying the obstacle geometry to a well-defined cubic shape in order to reveal the key fluid-dynamic mechanisms that occur when a rotor is hovering in its proximity.

The variation of the rotor performance was monitored by means of a six-component load cell. Laser Doppler Anemometry (LDA) measurements of the

rotor inflow were used in order to investigate how the aerodynamic interaction affected the rotor performance. Eventually Stereoscopic Particle Image Velocimetry (SPIV) measurements in the region between the rotor and the obstacle were carried out in order to have a better insight of the interacting flow field. Obstacle surface pressure measurements were also performed, and additional flow visualisation and PIV were performed in support of the pressure measurement tests.

2 Experimental Methods

2.1 Rotor loads, in-flow and wake survey

Four sets of experiments are described. These used two different rotor rigs and a small diameter thrusting propeller. All used obstacles of the same cube size as the rotor diameter. The small thrusting propeller system was used to obtain additional PIV for flow visualisation in support of the pressure data, and has not been described in any of the other Glasgow GARTEUR data.

The main features of the two rotor rigs are reported in Table 1. The collective blade pitch angle was fixed to 8°, whereas the lateral and longitudinal pitch were set to zero. The prescribed rotational speed was maintained during all the tests by means of a brush-less motor and was monitored from the motor speed feedback signal and with a stroboscope. No appreciable speed fluctuation (less than 1 *RPM*) was recorded during the tests. The two rotor rigs were used for different kind of measurements. In particular the Large rotor rig was used for the load measurements and the inflow LDA measurements, whereas the Small rotor rig was used to investigate the flow-field by means of Stereoscopic Particle Image Velocimetry (PIV). The operating conditions were such that the blade solidity and blade tip Mach number were the same for both the Large and Small rotor setups.

Both the Large and Small rotor rigs were characterised by an non-articulated, rigid, rotor hub, not allowing the flapping and lag blade motion which are quite difficult to be monitored on a small-scale model. In this way, the rotor geometry was *a priori* known and well-defined, while the general wake features were still representative of those of a real rotor. Owing to the presence of the flap hinges, a real rotor would experience less intense in-plane moment than those experienced by the considered fixed rotors, however the measured in-plane moments can still give a reasonable indication of how intense the interaction is for the different rotor position.

In addition, the choice of carrying out the experiments at fixed collective pitch

Table 1: Main features and operational conditions of the Rotor Rigs

Characteristics	Symbol	Large rotor rig	Small rotor rig
Cubic Obstacle size	L	1 m	0.3 m
Rotor diameter	D	1 m	0.3 m
Number of blades	N_b	4	2
Blade chord	c	53 mm	31.7 mm
Solidity	σ	0.135	0.134
Blade geometry		Untapered, untwisted	Untapered, untwisted
Collective pitch	θ_c	8^o	8^o
Rotor rotational frequency	Ω	1200 RPM (20 Hz)	4000 RPM (66.6 Hz)
Rotor rotational direction		clockwise	clockwise
Reynolds Number at blade tip	Re_{TIP}	220000	132000
Mach Number at blade tip	M_{TIP}	0.18	0.18
Type of Experimental investigation		Load measurement Inflow LDA measurements	Stereo-PIV

obviously prevents from carrying out a sensitivity analysis to the disk-loading, which represents an important parameter for the characterisation of the wake strength. However this analysis is beyond the purpose of the present work, i.e. to reveal the key fluid-dynamic mechanisms that occur in this kind of interaction, even though it is recommended for future investigations.

Two different reference systems are defined, as depicted in Fig. 1. The global reference system (X, Y, Z) defines the position of the rotor hub centre with respect to the obstacle, whereas the rotor reference system (x, y, z) coincides with the load-cell axes. The origin of the absolute (X, Y, Z) coordinate system is fixed and it is placed on the floor, at the obstacle mid-span, so that the X-coordinate represents the distance of the rotor centre from the obstacle, the Y-coordinate represents the distance of the rotor centre from symmetry plane and the Z-coordinate represents the height of the rotor centre from the ground.

The Large test rig was placed in a large laboratory space with an even, flat ground extending to a 5m radius away from the rotor centre line, corresponding to 5 rotor diameters. As previously stated, the Large rotor rig was instrumented with a 6-component load cell which allowed the measurements of the forces and moments generated by the rotor. The employed load cell was an AMTI MC36, whose amplifier was set at a very high sensitivity so that it would respond to the forces and moments. The nominal accuracy of the load cell was 0.25% of the

full-scale output, corresponding approximately to 0.5% of the measured thrust in Out of Ground Effect condition. The actual load measurements were obtained as the average of 5 runs, each of which was 2.5 s long. The reduced acquisition time was driven by the need of reducing the load-cell thermal drift.

In order to understand how the aerodynamic interaction affected the rotor performance, a measurement of rotor inflow was performed. In classical aerodynamics the in-flow velocity is treated as uniform across the disc and constant with time, but in practice the inflow is non-uniform and additionally unsteady due to the blade passing and wake effects. Inflow should be measured as close to the plane of the disk as possible, and consequently an optical method was preferred, but the requirement for unsteady flow measurement needs to be considered also. The rotor inflow measurements were carried out using a commercially available Dantec 2D FiberFlow two-component Laser Doppler Anemometry (LDA) system. A 112 mm diameter probe of 2 m focal length fitted with a beam expander allowed velocity measurements within a measurement volume ellipsoid of $2.62\text{mm} \times 0.12\text{mm} \times 0.12\text{mm}$. The probe axis was in the horizontal plane and was rotated by 45^{o} such that the LDA sensors responded to both vertical and horizontal velocity, and the inflow was calculated from an axis transformation. In anticipation of elevated turbulence levels in the obstacle flow case and to avoid the velocity-bias effect, the system was set to burst mode with transit (residence) time enabled for calculation of the mean flow velocity. Seeding was provided by a mineral oil based system that used a peristaltic pump to pump the oil through a heater matrix. The smoke oil had a substrate density 843kg/m^3 at room temperature, and the seeder unit manufacturer's calibration indicated a particle diameter of 0.2 to 0.3μm at the recommended heater operation temperature. During LDA operation a typical burst rate of 1000 to 2000 counts per second was achieved, equivalent to 50 to 100 counts per revolution. Sampling runs were performed to assess convergence for mean and root-mean-square velocity, and subsequently 7500 valid samples were taken at every measurement point, with absolute accuracy of approximately 0.02 m/s corresponding to 0.4% of the maximum inflow velocity. The LDA system was mounted on a 3D traverse system allowing positioning with accuracy of better than 0.1 mm. The LDA measurements were performed along the rotor x and y axes, 4 cm ($4\%D$) above the rotor plane, as represented in Fig. 2. Every LDA sweep comprised 101 evenly-spaced measurement points along the rotor diameter, allowing a spatial resolution of 10 mm ($1\%D$). The LDA measurements are defined in the rotor reference system (x, y, z). Hence, according to this convention, a positive induced velocity points downwards.

Stereoscopic PIV was used to investigate the flow in the region between the

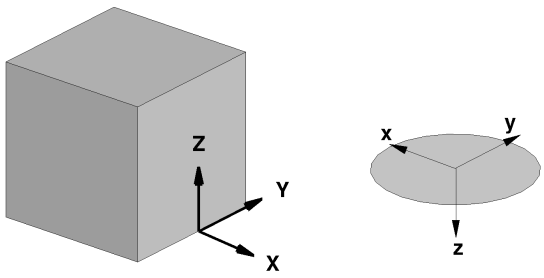

Figure 1: Global (X, Y, Z) and Rotor (x, y, z) reference systems.

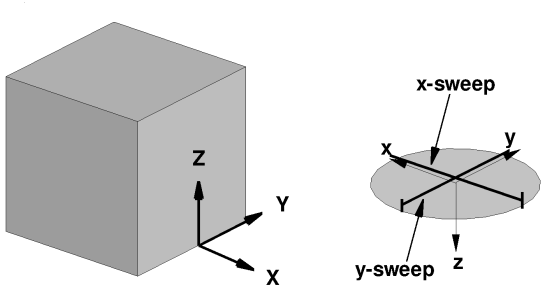

Figure 2: Position of the LDA measurement points along the rotor x and y axes.

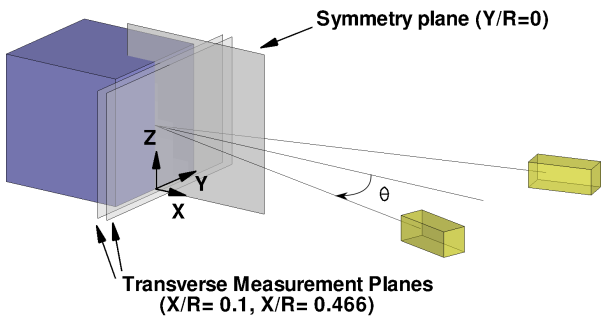

Figure 3: PIV setup and measurement planes

obstacle and the rotor using the Small rotor rig. These measurements were carried out in the University of Glasgow deHavilland wind tunnel, which has a 2.66 m wide x 2.07 m high (8.9×7 rotor diameters), by means of a LaVision system running Davis 8. The wind tunnel was not run during the experiments. PIV images were acquired by two Phantom v341 cameras, whose resolution was 4Mpixel. The seeded flow was illuminated by a Nd:YAG laser capable of 100mJ pulses at a maximum repetition rate of 200 Hz, however the sample rate was actually set to 197 Hz in order to prevent phase-locked measurements at 0^o, 120^o and 240^o and have a statistically representative database of the different blade phases. The ensemble-averaged measurements over 500 image pairs are presented in this paper. The cameras, which were placed on the same or either side of the laser sheet, depending on the investigated plane, were equipped with Scheimpflug adaptors and an angle separation of 29.6 degrees was used. Calibration was performed using a 3D calibration plate and Davis 8 software. Atomised oil based seeding for the PIV system was used with nominal particle diameter less than $1\mu m$. The image pairs were post-processed by means of the Davis 8 software using 32×32 pixels interrogation windows with an overlap factor of 50%.

Three measurement planes were investigated, as represented in Fig. 3:

- The symmetry plane ($Y/R = 0$). In this PIV configuration, the cameras were placed on either side of the laser sheet. The uncertainty of the velocity measurement was estimated to be $\epsilon_u = \frac{1}{\sqrt{2}} \frac{0.1}{M\Delta t} = 0.1\ m/s$ for the in-plane velocity components and $\epsilon_{u,\mathrm{op}} = \frac{1}{\sqrt{2}\tan\theta} \frac{0.1}{M\Delta t} = 0.33\ m/s$ for the out-of-plane component, assuming a maximum displacement error of 0.1 pixels since a gaussian sub-pixel interpolation algorithm was used. An optical magnification factor of M =3.4161 pixel/mm was obtained through the calibration process, together with a pulse separation time of $\Delta t = 200\ \mu s$ and $\theta = 14.8°$, corresponding to half of the camera separation angle, as represented in Fig. 3.

- Two transverse planes with different distance from the obstacle, namely $X/R = 0.1$ and $X/R = 0.4666$. In this PIV configuration, the cameras were placed on the same side of the laser sheet. The uncertainty of the velocity measurement was estimated to be $\epsilon_u = 0.07\ m/s$ for the in-plane velocity components and $\epsilon_{u,\mathrm{op}} = 0.23\ m/s$ for the out-of-plane component, since an optical magnification factor of M =4.85 pixel/mm resulted from the PIV calibration.

2.2 Obstacle surface pressure measurements and additional flow visualisation

The small rotor rig was also used in the large, empty laboratory for surface pressure measurements and flow visualisation with a smoke wand. A total of 180 pressure tappings were installed on the top and one side (front) of the cube obstacle, distributed as shown in figure 14. The pressure tappings were connected by 0.15m flexible tubes to a Scanivalve ZOC23B pressure scanner with ±2.5kPa range. The pressure scanner is capable of responding to very high speed unsteady pressure signals for a single channel (>10kHz) if arranged appropriately, but the sampling rate per channel is less when multiplexing over multiple channels, and in this case the sampling rate was set to 625Hz per channel. The long connecting tube has the effect of attenuating and phase shifting the unsteady pressure, but this would be identical for each tapping. Calibration tests indicated that the scanning module sensors would respond to pressure changes less than 0.1Pa, equivalent to a C_p error of 0.0004 with the scaling used in this paper. The rotor and obstacle were situated in the middle of a large, unventilated room with a flat, horizontal floor, and a 6m ceiling height, and there were no floor obstructions over a radius of at least 10 rotor diameters. The test laboratory therefore had no ambient flow, and any recirculation of flow into the rotor would have been due to obstacle effects only and not a consequence of the test environment.

Finally an additional set of limited PIV experiments were done using a two-component PIV system in a 1m x 1m sized working section wind tunnel with the tunnel not running. A 15cm diameter propeller was used for the rotor system, and a 15cm cube was used as the obstacle. This additional PIV was done in support of the pressure measurements. PIV images were sampled using a Redlake Megaplus 4 4MPixel camera, and image analysis was done using matpiv, an open source PIV library. These PIV tests were done to provide additional qualitative flow visualisation.

2.3 The Test Matrix

The experimental campaign consisted of a set of tests reproducing hovering flight conditions at several rotor positions with respect to a simplified obstacle with a cubic shape.

The text matrix for the loads measurements is represented in Fig. 4, where each circle represents the position of the rotor hub centre for that particular test. It consists of several measurement points at the heights of $Z/R = 1, 3/2, 2, 3$ and

4. The measurements were carried out placing the rotor in two different planes:

- $Y/R = 0$, corresponding to the plane symmetry test.
- $Y/R = 1$, corresponding to a plane tangent to the obstacle lateral face.

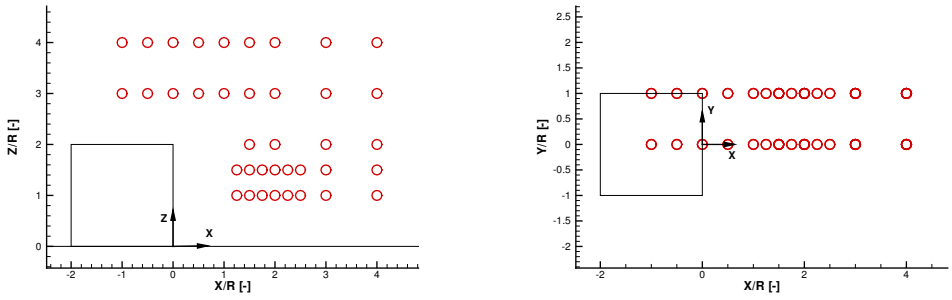

(a) Test Points - Lateral View

(b) Test Points - Birdseye View

Figure 4: Test Points. Each circle represents the position of the rotor hub centre for that particular Test Point.

The loads and moments will be expressed according to the rotor reference system (x, y, z). Hence a positive M_y moment is equivalent to a pitching nose-up moment if a helicopter was facing the wall. Similarly, a positive M_x moment is equivalent to a roll moment that promotes a thrust rotation towards the positive y-coordinate.

The LDA measurements were carried out in a subset of the measurement points of Fig. 4, i.e. those at $Z/R = 3/2$ and 3, due to the maximum and minimum height achievable by the traversing system. The Stereo-PIV measurements were carried out just for the test points at which the rotor was positioned in the symmetry plane, i.e. $Y/R = 0$. In particular the symmetry plane $Y/R = 0$ was investigated for the rotor positions X/R and Z/R varying from $3/2$ to 3, whereas the two transverse planes were acquired just for $X/R = 3/2, Z/R = 2$ and $X/R = 2, Z/R = 2$.

The obstacle upper and front surface pressures were measured for the configurations shown in table 2. The pressure scanner was zeroed before each experimental run following a 60 second period with the rotor was at rest. The rotor was brought up to its operating rotational speed, and measurements were recorded after 20 seconds to allow transients to decay. Measurements were recorded at a

Table 2: Table of experimental configurations for surface pressure measurement, x indicates measured configurations.

Height $\frac{Z}{R}$	**Lateral Displacement** X/R											
	−1.0	0.0	0.50	1.0	1.5	1.0	3.0	4.0	5.0	6.0	7.0	8.0
3.86	x	x	x	x	x	x	x	x	x	x	x	x
2.86	x	x	x	x	x	x	x	x	x	x	x	x
2.0	-	-	-	-	x	x	x	x	x	x	x	x
1.0	-	-	-	-	x	x	x	x	x	x	x	x

frequency of 625Hz for 4.8s for each pressure tapping location.
Smoke flow visualization was used to examine the structure of the rotor wake. Oil based smoke was introduced into the airflow at the end of an electrically heated smoke wand, and this allowed both the blade tip vortices and the structure of the rotor wake/obstacle interaction to be visualised. A high energy, $1\mu s$ pulse width stroboscope was used with a digital video camera running at 133 frames per second for illumination and digital video recording. Smoke was entrained into the vortex wake by positioning the smoke wand close to the edge of the rotor disc, and the vortex cores were clear for five or so helix windings until turbulent diffusion of the smoke led to the rapid loss of definition of the vortex filaments.

The obstacle upper and front surface pressures were measured for the configurations shown in table 2. The pressure scanner was zeroed before each experimental run following a 60 second period with the rotor was at rest. The rotor was brought up to its operating rotational speed, and measurements were recorded after 20 seconds to allow transients to decay. Measurements were recorded at a frequency of 625Hz for 4.8s for each pressure tapping location.

3 Results and discussion

3.1 LDA, loads and stereo PIV investigation

In this section the main results of the experimental survey will be analysed. The load measurements for the different rotor position are presented in Fig. 6,7 and Fig. 8, while the LDA inflow measurements along the x and y rotor-axes are presented in Fig. 9 and 10. The PIV measurements in the symmetry plane $Y/R = 0$ are presented in Fig. 11 (in-plane velocity magnitude contours and streamlines), while the transverse planes are presented in Fig. 12 and 13.

A set of load measurements were initially carried out in order to quantify the rotor performance in absence of the obstacle. The rotor was placed as high as possible ($Z/R = 4$) in order to assess the Out-of-Ground-Effect (OGE) condition. A $c_{T,\mathrm{OGE}}$ of $7.36 \cdot 10^{-3}$ and a $c_{Q,\mathrm{OGE}}$ of $8.75 \cdot 10^{-4}$ were obtained, leading to a Figure of Merit of $FM_{\mathrm{OGE}} = 0.51$, as summed up in Table 3.

Table 3: Out-of-Ground-Effect (OGE) reference condition

$c_{T,\mathrm{OGE}}$	$7.36 \cdot 10^{-3}$
$c_{Q,\mathrm{OGE}}$	$8.75 \cdot 10^{-4}$
FM_{OGE}	0.51

All the results for the thrust coefficient and figure of merit will be presented from now scaled by their respective OGE values, in order to appreciate their variation from the reference condition, while the moment coefficients c_{Mx} and c_{My} will be presented through their ratio with $c_{Q,\mathrm{OGE}}$, so that they are expressed as fraction of the OGE torque.

The results of the Ground Effect test, positioning the rotor at different height in absence of the obstacle, are shown in Fig. 5. The typical thrust increase, up to 20% of the OGE value, can be recognised as the rotor is positioned closer to the ground.

3.2 Results, rotor placed in the symmetry plane $Y/R = 0$

This section presents the results of the test where the rotor axis was placed in the obstacle symmetry plane $Y/R = 0$. Variation of the thrust coefficient with respect to the out-of-ground-effect (OGE) condition is presented in the plots of Fig. 6a, 6b and 8a. The typical thrust increase (up to 20%) due to the ground effect can be observed in both the region over the centre of the obstacle and far from the obstacle, since the relative distance to the closest surface (either the floor or the top of the obstacle) is the same ($1R$) and the rotor projection lies completely on the obstacle top face. The comparison between the variation of the thrust coefficient above and far from the obstacle is presented in Fig.5, showing that the extent of the finite ground plane necessary to produce IGE performance benefits does not to be much bigger than the the projected area of the rotor. However two main regions where the rotor performance deviates from the nominal behaviour can be observed.

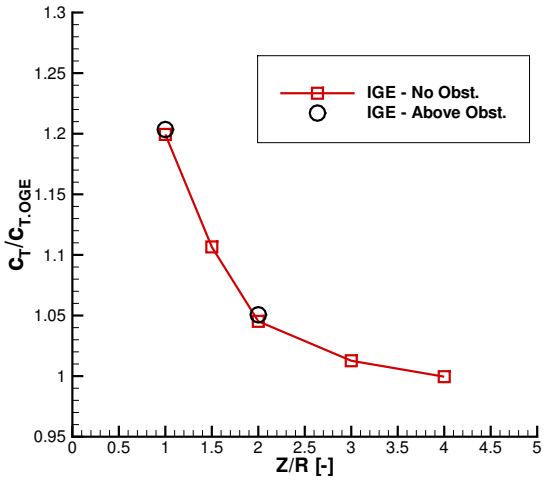

Figure 5: Ground effect test in absence of the obstacle (red markers) and above the obstacle ($X/R = -1$, black markers). The latter data have a Z/R offset equal to the obstacle height (2).

The first region is the one above the edge of the obstacle, where the thrust coefficient decreases as the rotor is positioned outwards, owing to the minority of the rotor lying over the upper surface of the obstacle. This phenomenon can be appreciated also in the inflow profile of Fig. 9a measured by means of the LDA system. In this case a gradual reduction of the inflow velocity is observed going from $X/R = 1$ to $X/R = -1$, as prescribed by the ground effect. However, one would expect this variation to be non-symmetrical, since only part of the rotor projection lies on the top of the obstacle and thus is affected by the ground effect. However this appears not to be the case since the inflow profiles of Fig. 9a remain approximately symmetrical as the rotor is placed in the different positions above the obstacle. This is also reflected by the fact that the the pitch and roll moments of Fig. 7a and 7c are quite close to zero in the region $-1 < X/R < 1$. An additional interesting moment behaviour can be observed moving the rotor away from the obstacle ($1 < X/R < 3$) at the same heights ($Z/R = 3, 4$), where a positive $y-$moment develops on the rotor, which disappears farther outboard ($X/R > 4$).

The second region, probably of more interest, is the one just beside the obstacle ($1 < X/R < 3$, $1 < Z/R < 3$), where a severe ground effect reduction can be observed (Fig. 6b), since the thrust coefficient drops to a value slightly below

the OGE one, even at low heights. This behaviour is caused by the development of a recirculation regime in the region between the rotor and the obstacle. The rotor wake, once deflected by the ground, is deflected again by the obstacle and then re-ingested by the rotor itself. This recirculation region, which is evident in the PIV flow-fields of Fig. 11, causes an increased induced velocity and a consequent loss of thrust, similar to a partial vortex ring state. This effect is deeply dependent on both the rotor height and distance from the obstacle. A maximum thrust loss of 8% with respect to the furthest rotor position at the same height can be observed at $Z/R = 1$ and $3/2$, whereas at $Z/R = 2$ the maximum thrust loss is lower (approximately 4 %). Moreover one can appreciate the fact that the thrust loss is not monotonic when getting closer to the obstacle, but it presents a local minimum at approximately $X/R = 2$. This can be explained looking at Fig. 11, where at $X/R = 2$ (Fig.11d, 11e, 11f) the upwards in-plane velocity close to the front face of the obstacle (the green layer) is higher than in the other cases (approximately 4 m/s instead of 2.5), thus implying a stronger recirculation. In the other cases (further and closer to the obstacle) most of the air flows on the side of the obstacle instead of being redirected upwards. The effects of the obstacle start to be negligible when the rotor is further than 4 radii from the obstacle itself.

Another important feature of this region is the appearance of a strong nose-down pitching moment (up to 30% of the measured torque, Fig. 8g). This is due to the fact that the previously-introduced recirculation region mainly affects the portion of the rotor closer to the obstacle as it is shown in Fig. 9c, where an increased induced velocity can be observed in the left portion of the inflow profile for $X/R = 3/2$. Consequently, a negative c_{My} moment is generated on the rotor, which is evident in Fig. 7d and 8g for $Z/R = 3/2$ and $Z/R = 2$ close to the obstacle, which is equivalent to a nose-down pitching moment if a helicopter was facing the wall. A roll moment, even if with a much smaller value with respect to the $y-$moment, develops as well in the region on the side of the obstacle, as can be seen in Fig. 7b and 8e, even if with a much smaller value with respect to the $y-$moment. This behaviour can be explained by the different composition of the horizontal velocity arising from the recirculating cell with the advancing and retreating blade, causing a different loading between the left and right side of the rotor.

With reference to rotor efficiency, quite limited variations of the torque coefficient were observed among all the rotor positions (less than 4%), leading to a Figure of Merit behaviour (Fig. 6c and 6d and 8c) that is very similar to the thrust coefficient one.

In order to reveal the main features of the flow-field in the symmmetry plane

$Y/R = 0$, the in-plane velocity magnitude contours and streamlines are presented in Fig. 11. As we can appreciate, the recirculation region is present in all the cases, even though its morphology is highly case-dependent. At $X/R = 3/2$ (Fig. 11a, 11b, 11c) the rotor slipstream does not impinge on the floor before being deflected towards the obstacle, but impinges directly on the obstacle. This is due to the formation of a counter-rotating (with respect to the main one) recirculation region on the floor. This region is pushed towards the obstacle as the rotor is moved downwards. At $X/R = 2$ (Fig. 11d, 11e, 11f), as already highlighted in the previous paragraphs, the rotor wake impinges on the floor before being deflected by the obstacle and re-ingested by the rotor. The air-layer that goes upwards close to the obstacle is thicker and faster than the other cases, probably indicating a stronger interaction with the rotor (confirmed, as previously stated, by the thrust measurements). Eventually at $X/R = 3$ (Fig. 11g, 11h, 11i) the flow pattern is very similar to a non-disturbed rotor wake in ground effect, suggesting that the interaction in this case is weaker (as the load measurements also confirm).

Two transverse planes at $X/R = 0.1$ (close to the obstacle) and $X/R = 0.466$ (close to the rotor) were also investigated by means of PIV in order to have a deeper insight of the recirculating flow field, for two different rotor positions: $X/R = 3/2$, $Z/R = 2$ (Fig. 12) and $X/R = 2$, $Z/R = 2$ (Fig. 13).

Consider first the plane at $X/R = 0.1$. When the rotor is positioned at $X/R = 3/2$, the rotor wake directly impinges on the lower part of the obstacle, as previously appreciated in flow-field in the symmetry plane of Fig. 11c. There is also evidence in Fig. 12a, where the upper part of the obstacle is affected by the upwards velocity of the recirculation region, whereas the lower part presents a downwards velocity. This phenomenon is not present anymore when the rotor is placed further from the building as presented in Fig. 13a, since the rotor wake impinges on the floor before being deflected towards the obstacle. In both cases the out-of plane velocity component is almost null due to the obstacle blockage effect. Part of the rotor wake is not deflected by the obstacle, but it skims its lateral faces as highlighted by the two regions on the side of the building characterised by a higher out-of-plane velocity.

The second transverse PIV measurement plane at $X/R = 0.466$ directly slices the rotor wake, which can be recognised as the blue high out-of-plane velocity region. However since the position of the measurement plane with respect to the obstacle is the same for the two cases but the rotor position varies, the two slices represent different regions of the rotor wake. In the first case (rotor at $X/R = 3/2$), the plane is closer to the rotor, therefore the wake is sliced in at a higher position (Fig. 13a), whereas in the second case (rotor at $X/R = 2$), the wake has already

impacted on the floor and it is going towards the obstacle as can be appreciated in Fig. 13b.

3.3 Results, rotor placed out of the symmetry plane, $Y/R = 1$

The effect of placing the rotor at $Y/R = 1$, out of the symmetry plane of the problem, is analysed in this subsection. As in the previous case, two main regions where the rotor performance deviates from the nominal behaviour can be observed: the region above the edge of the obstacle and the one on the side of the obstacle.

In the first region, a gradual ground effect can be observed as the rotor is moved over the obstacle, similarly to the tests at $Y/R = 0$. However the observed ground effect is weaker as can be appreciated in Fig. 6a and 8b, due to the fact that in the innermost postion $X/R = -1$, just half of the rotor projection lies on the upper surface of the obstacle. This is also evident when comparing the LDA inflow measurements of Fig. 9a and 9b: the reduction in the induced velocity is less intense when the rotor is placed at $Y/R = 1$. However, as for $Y/R = 0$, the inflow profiles remain almost symmetrical, leading to very small x and y moments in the region $-1 < X/R < 1$ (Fig. 7a and 7c).

In the second region, the one on the side of the obstacle, the effect of the flow recirculation on the rotor performance becomes less intense with respect to the tests at $Y/R = 1$, according to the fact that only half rotor faces the obstacle. The thrust coefficient reduction is less pronounced as the rotor is placed closer to the obstacle, as can be appreciated in Fig. 6b. Consequently also the $y-$moment generated in this region is less intense (Fig. 8h). However, since just the negative $y-$portion of the rotor (if we consider a helicopter facing the obstacle) is affected by the recirculating flow, a negative $x-$moment is generated on the rotor, as can be appreciated in Fig. 7b. If we imagine a helicopter facing the obstacle, this moment corresponds to a roll moment that promotes a thrust rotation to the left.

3.4 Surface pressure distributions

Contour maps of the mean coefficient of pressure $-C_p$ have been plotted onto the front and top surfaces of the cuboid obstacle to give an overview of the loading distributions. Pressure coefficient is scaled with $\frac{1}{2}\rho V_{TIP}^2$. Results are shown in figures 17, 18 and 19 for $3.86R$, $2.86R$ and $2R$ rotor height respectively. For figures 17 and 18 rotor obstacle spacing increases from frame (a), with the rotor directly above the centre of the obstacle, to frame (i) at $X/R = 8$. High positive pressure

on the upper surface is observed for all cases where the rotor disc overlaps with the upper surface of the obstacle, and the pressure is higher if the rotor is closer to the obstacle surface. Frame (b) of both figures at $X/R = 0$ shows an interesting crescent shaped band of high pressure. Flow visualisation for $3.86R$ rotor height for this configuration is shown in figure 30, where the spreading out of the smoke has been annotated for clarity. The high pressure is due to the direct impingement of the wake vortices onto the surface, and the crescent shape is a consequence of the subsequent spreading out of the wake flow over the upper surface. Frame (b) at the lower rotor height, figure 18, shows a similar feature but with higher pressure. Frame (d) of figures 17 and 18 is for rotor spacing $X/R = 1.0$, and suction can be see on the top surface and positive pressure can be seen on the front surface. PIV showed entrained flow over the upper surface towards the rotor (frame (b) of figure 27), and both flow visualisation (figure 31) and the PIV show the wake passing down the side of the obstacle at this spacing. The induced flow towards the rotor causes the suction on the upper surface, and the wake flow down the side causes the high positive pressure around the ground/ obstacle edge. The effect is greater at the lower rotor height due to the increased confinement of the wake by the ground and the obstacle. Flow visualisation and PIV showed the development of the recirculation zone between the obstacle and the rotor as the obstacle was moved even farther outboard, and the subsequent pressure distributions in frames (e) to (h) of these figures show high pressure associated with the impingement of the recirculation on the ground/ obstacle edge, and lower pressure higher up as the flow accelerates towards the top surface. Frame (i) on both figures shows notionally ambient pressure on both the upper and front surfaces at the obstacle distance $X/R = 8$. Figure 19 shows pressure distributions for rotor height $2R$, and obstacle locations from $X/R = 1.5$ outboard are shown. The upper surface pressure shows only weak suction, and this will be due to rotor inflow and wake recirculation. The front face shows high positive pressure at the ground/ obstacle edge with suction higher up, and this is due to the recirculation zone set up between the rotor, ground and obstacle. At lower rotor heights more intense pressure is observed on the obstacle front face.

Integration of the surface pressure distributions reveals the surface forces, and figures 20 and 21 show these forces for the top and front surfaces respectively. The forces have been scaled with the rotor thrust T, and the plots show the variation of the force with rotor height and distance of the rotor from the obstacle. Figure 20 for the top surface shows a high positive (down) force when the rotor is directly above the obstacle, and this force reduces rapidly to a negative (upwards) force at $X/R = 1.0$ when the rotor disc edge is above the obstacle edge. The forces

have stronger magnitude at the lower rotor height. The positive force when the rotor overlaps the upper surface is due to the direct wake impingement, and the suction is due to the induced flow over the upper surface by the wake movement down the side. As obstacle distance increases the net force becomes negligible, and the rotor and wake are too far from the obstacle top to have any significant effect. Forces on the front face, figure 21, are lower in magnitude and have a more dramatic variation. A positive force is towards the obstacle. When the rotor is directly over the obstacle the side force is almost zero, but movement of the obstacle results in maximum side force at $X/R = 0.50$. This is part way between the cases when the wake impinges directly onto the upper surface at closer obstacle spacing, or passes down past the front face at higher obstacle spacing. The highest positive pressure is observed at the obstacle/ ground corner in this case. It was not possible to do PIV for this case because of excessive shadow beneath the rotor hub, but the flow visualisation results suggest the high positive pressure at the ground is the result of passage of wake flow down the side of the obstacle and its subsequent impingement on the ground. At higher obstacle spacing the wake vortices impinge on the ground (as revealed by the PIV), so the side force is low, and as obstacle spacing increases further the recirculation builds up, causing an increase of side force that diminishes to zero as the obstacle distance increases and the recirculation becomes less energetic. When the rotor disc is below the plane of the upper surface, the side force is initially weak at close obstacle spacing, and becomes positive as the recirculation zone builds up. The rotor wake/ obstacle interaction is fundamentally an unsteady process. Root mean square (RMS) of the time varying pressure signal relative to the mean pressure has been calculated from the pressure data, and representative RMS pressure distributions are shown on figures 22 and 23 for the top and front faces respectively. The top surface RMS pressures, figure 22, are for rotor height $2.86R$. High RMS signals on the top surface are only observed when the rotor disc overlaps with the top of the obstacle. The impingement of the rotor vortices on the top surface is shown by the curved arc of high RMS pressure, while low RMS pressure is observed around the rotor axis location. Particularly strong RMS pressure levels are seen for the obstacle spacing $X/R = 0.5$, and in this case the wake vortices impinge close to the upper edge of the obstacle. At this obstacle position, high RMS pressures are observed along the top line of pressure tappings on the front face also. At higher rotor/ obstacle spacing the RMS pressure on the upper surface becomes very low as the wake impingement ceases. Note that the RMS pressure levels are about one third of the level of the mean pressure, so the local unsteady loading is significant. PIV data on figure 27 shows the rotor wake trajectory at this rotor height for rotor spac-

ings X/R =-1 with wake impingement on the top surface and X/R =1.0 without wake impingement on the top surface, and these would help to explain the RMS pressure distributions. Figure 23 for the front of the obstacle shows three rotor heights for rotor spacing X/R =1.5. Frame (a) for this figure is for rotor height Z/R =2.86, and the RMS signal shows a moderate unsteady pressure just above the obstacle/ ground edge. Frame (b) for the lower rotor height Z/R =2.0 shows a much higher unsteadiness in the pressure signal, the reason for this being the greater confinement of the rotor wake due to the lower rotor height, and frame (c) for Z/R =1 shows even greater RMS signal again. The front face shows the strongest signal around the obstacle/ ground edge, where wake impingement on the front face occurs, and this in turn is stronger at the lower rotor height. The unsteadiness of the signal is driven by the gross recirculation set up between the rotor, ground and obstacle front face, and this carries the wake vortices towards the obstacle and up the front face, see figure figure 27. At high obstacle spacing, the RMS signals are low, and this is due to the attenuation of the wake vortices caused by their spreading out over the ground and the turbulent diffusion of the vorticity.

The pressure signal underlying the unsteadiness is interesting to consider. The case with the rotor at height 2.86R with obstacle spacing X/R =0 (figure 22 frame (b)) is chosen as there is significant overlap between the rotor disc and upper surface and a wide distribution of high RMS pressure.. Pressure spectra for three surface tapping locations along the centre-line of the top surface at x/D = 0.38, 0.70 and 0.92 are shown in figure 24. The flow visualisation image at rotor height Z/R =3.86 shown in figure 30 is appropriate for the pressure data case shown; after impacting on the upper surface of the obstacle, the flow visualisation shows the vortex wake passing over the upper surface away from the rotor axis, see figure 30. Figure 24 frame (a) showing the spectral analysis at x/D = 0.38 shows two peaks, one at the blade passing frequency (non-dimensional frequency 2), and a smaller peak at 2.3 $\times$ the rotational speed. Note there are two very weak peaks at 3.6 and 3.7 $\times$ the rotational frequency. This frame is early on in the surface/ wake interaction. Frame (b) is later and further outboard at x/D = 0.7, and many more spectral peaks are observed. Firstly there are the same sets of frequencies as with frame (a), but the higher frequency peaks are now much stronger, but a peak at 4 $\times$ the rotational frequency is observed, and lower frequency peaks at 1.3 and 1.7 $\times$ the rotational frequency are seen also. Note that the RMS pressure plotted in figure 22 shows higher signal RMS at x/D =0.7 compared to x/D =0.3 for this rotor spacing. Finally the most outboard location at x/D = 0.92 shows only weak peaks at 2, 3.6 and 3.7 $\times$ the rotational frequency. The pressure scanning

modules were on the end of long tubes, but the attenuation and phase shift effect would be the same for each tapping location. Figure 25 shows selected spectra with the obstacle spacing X/D =0.5 for the same rotor height, but with pressure tappings at x/D =0.17, 0.38 and 0.7, and the reader should refer to figure 22 again for the RMS pressure at this rotor spacing. Again the vortex track is outboard away from the rotor axis, and the spectra show remarkably similar development to those for the X/D =0 obstacle spacing in the previous figure. Frames (a) and (b) of figure 24 and frames (b) and (c) of figure 25 are in fact the same two respective tapping locations, and note that frame (b) of each figure are at almost the same distance from the rotor axis and the RMS levels are both very high. The change in spectral content with the wake development over the upper surface reveals a highly non-linear interaction, but note that the wake/ upper surface interaction is very different from the interaction with a plane ground in that the latter extends to infinity also. A vortex stretching effect will be significant in the interaction with the obstacle upper surface as the wake vortices are still relatively young.

3.5 Additional PIV and Smoke Flow Visualization

Mean flow velocity plots are presented in figure 26 through to figure 28. During PIV data collection the camera was located with reference to the obstacle front surface therefore the size of the investigation area changed for each experimental configuration. For figure 26 frame (a) with rotor height $1.93D$ above the ground and no obstacle, the classical ground effect wake configuration can be seen, with the wake broadening as the flow approaches the ground before the high momentum flow spreads radially outward. Frame (b) shows the obstacle at X/D=-0.5, with the rotor axis directly above the centre of the obstacle. The upper surface of the obstacle presents a zone of enhanced ground effect, and the flow spreads out as it approaches the obstacle upper surface, but after the wake shear layer passes over the edge of the upper surface it then proceeds downwards at a shallow angle. A gentle recirculation is induced between this strong shear layer, the obstacle side face and the ground, and this is shown by the streamlines on the PIV plot. The wake shear layer itself is a highly unsteady flow because it contains the trailed tip vortices, so the impingement of this shear layer on the obstacle is expected to induce strong, unsteady pressure signals in that vicinity. Frame (c) of this figure shows the obstacle outboard at X/D=1.0. The rotor wake impinges on the ground and spreads out in a similar way to frame (a), but the presence of the obstacle prevents the further radial spreading of the wake and deflects the wake flow upwards. The PIV shows a strong variation of mean velocity on the side of the obstacle

from the ground upwards, with very low mean velocity at the ground, suggesting high pressure, and velocity increasing further up, suggesting a fall in pressure in that direction. The mean flow streamlines suggest a gentle recirculation between the rotor and the obstacle face. Figure 27 shows two obstacle spacings with the rotor height $1.43D$. Frame (a) with the rotor axis directly above the centre of the obstacle can be compared with figure 26 frame (b) for the higher rotor height. The wake velocities are larger at the lower rotor height, but the overall features are similar. Frame (b) of figure 27 shows the obstacle at X/D=0.5, so the edge of the rotor disc is directly over the edge of the obstacle. As the wake approaches the ground the presence of the obstacle prevents it from spreading out radially, instead the obstacle face and the momentum due to the remainder of the rotor wake flow deflects the flow into the out-of-plane direction, which cannot be detected with the two-component PIV. Flow is drawn over the top of the obstacle towards the rotor wake, and this flow then turns *downwards* to pass over the vertical face of the obstacle due to the entrainment of the rotor wake. Finally figure 28 shows the rotor at height 1D above the ground, showing the flow without the obstacle and the flow with the obstacle at X/D=1. Compared to the higher rotor height in figure 26 for the same obstacle spacing distance, the wake velocity is higher, velocity magnitude close to the obstacle face is greater, and the recirculation between the obstacle face and the rotor appears to be stronger.

Smoke flow visualisation was most effective when the smoke wand was positioned to permit smoke entrainment into the vortices as they formed. Figure 29 shows a typical rotor wake visualisation with the rotor at $1.93D$ above the ground and the rotor axis directly over the centre of the obstacle. Feature (i) shows the vortex cores, (ii) is the rotor, (iii) is the swan neck of the smoke wand. Faint wisps of smoke can be seen to the left of the vortex cores, and these are the helical vortex filaments. This figure shows the trajectory of the vortex cores down towards the obstacle surface, suggesting that the vortex cores impinge on the obstacle edge. Figure 30 shows the rotor at height $1.93D$, but with the obstacle at $X/D = 0$. The image again shows a freshly formed vortex core, the vortices passing down towards the obstacle, but the smoke trajectory at the obstacle upper surface is outboard, (ii), indicated by the arrow. The wispy, helical vortex filaments are clearly visible in this image, (i). Figure 31 with he rotor at $1.93D$ and the obstacle at $X/D = 0.5$ now shows the vortices passing to the left of the obstacle edge and down past the vertical face. Figure 32 with the rotor at a lower height and the rotor axis directly above the centre of the obstacle, shows the rotor wake impingement on the obstacle edge; a young vortex is shown springing from the edge of the

rotor disc, and the smoke shows the track of the vortex filaments, with (ii) indicating an aged, deflected vortex after it has passed over the edge. The trajectory of the smoke is reflected in the mean flow streamlines of the PIV in figure 27 frame (a). Finally figure 33 shows a highly distorted vortex filament (ii) that has passed over the corner of the obstacle; at this rotor height the vortices are relatively young when they impinge on the obstacle edge, and without the obstacle present the vortices would present as smoothly curved helical filaments. Filament distortion due to interaction with the corner of the obstacle is evident in this picture.

4 Conclusions

A comprehensive experimental survey of the aerodynamic interaction between a rotor and a model ground obstacle has been described. The experimental activities, carried out at University of Glasgow, took advantage of two rotor rigs and several experimental techniques. Load measurements on the rotor were carried out in order to assess the rotor performance for different rotor positions with respect to the obstacle. Laser Doppler Anemometry (LDA) measurements of the rotor inflow were used in order to see how the aerodynamic interaction affected the rotor performance. Particle Image Velocimetry (PIV) measurements in the region between the rotor and the obstacle were carried out in order to have a better insight of the interacting flow field. Surface pressure measurements and flow visualisation experiments were performed also.

The investigation examined two scenarios of interest to pilots: flying over the object and flying on the side of to the object. The first region of interest, corresponding to the first scenario, is the one above the edge of the obstacle, where the rotor experiences a gradual ground effect as it is positioned over the obstacle. In this case also a gradual reduction of the inflow velocity is observed, as prescribed by the ground effect. Since only part of the rotor is over the obstacle, one would expect the inflow to be non-symmetrical. However, it results to be indeed symmetrical, leading to the generation of almost null pitch and roll moments. When the rotor is completely over the obstacle the experienced ground effect is equivalent to the one measured with an infinite surface underneath, showing that the extent of the finite ground plane necessary to produce IGE performance benefits does not to be much bigger than the the projected area of the rotor.

The second region, probably of more interest, is the one just beside the obstacle where a recirculation region between the rotor and the obstacle develops. Its morphology is deeply dependent on the rotor position. This recirculation region

implies a severe thrust loss (up to 8%) with respect to the one without obstacle at the same height, implying that pilots should not plan for IGE augmented performance when landing close to a vertical obstacle, since that augmentation can be robbed by adverse interactions with obstacle itself. This thrust loss has a maximum at approximately 2 radii from the obstacle. Another important feature of this region is the development of strong pitching and rolling moments (up to 30% of the measured torque), due to the non symmetrical inflow pattern on the rotor. When the rotor is positioned out of the symmetry plane of the problem, the effect of the flow recirculation on the rotor performance becomes less intense, owing to the fact that only half rotor faces the obstacle. Consequently also the pitch-moment generated in this region is less intense.

Limited torque variations were observed throughout the testing, leading to the fact that the rotor figure of merit varied mostly according to the thrust coefficient. The obstacle influence on the rotor appears to be negligible when the rotor is more than 4 radii away from the obstacle. An investigation of rotor wake interactions with an obstacle has been performed. The phenomena are driven by the convecting rotor wake vortices and their deflection due to the ground and obstacle surfaces. Obstacle top and side surface forces are dependent upon the rotor height and obstacle to rotor spacing, and the forces diminish to zero at large rotor/ obstacle spacing. The top surface experiences a significant downward force when there is large overlap with the rotor disc, and intense vortex-edge interactions occur when the rotor trailing vortices pass directly onto the edge. The force on the obstacle front face is lower in magnitude, and the pressure loading is most intense at the upper edge and the ground/ obstacle edge. Unsteady loading is present due to wake impingement on the obstacle surfaces, and spectral analysis of the unsteady pressure signals reveal a rapidly evolving vortex/ surface interaction.

Obstacle top and side surface forces are dependent upon the rotor height and obstacle to rotor spacing, and the forces diminish to zero at large rotor/ obstacle spacing. The top surface experiences a significant downward force when there is large overlap with the rotor disc, and intense vortex-edge interactions occur when the rotor trailing vortices pass directly onto the edge. The force on the obstacle front face is lower in magnitude, and the pressure loading is most intense at the upper edge and the ground/ obstacle edge. Unsteady loading is present due to wake impingement on the obstacle surfaces, and spectral analysis of the unsteady pressure signals reveal a rapidly evolving vortex/ surface interaction.

ACKNOWLEDGEMENTS

Pressure measurement and flow visualisation instrumentation used for this project was provided by the National Wind Tunnel Facility funded by EPSRC, grant number EP/L024888/1. The work forms part of the GARTEUR AG22 project "Forces on obstacles in a rotor wake".

References

[1] G. Gibertini, D. Grassi, C. Parolini, D. Zagaglia, and A. Zanotti. Experimental investigation on the aerodynamic interaction between a helicopter and ground obstacles. *Proceedings of the Institution of Mechanical Engineers, Part G: Journal of Aerospace Engineering*, 229(8):1395–1406, 2015.

[2] N. Iboshi, N. Itoga, J. Prasad, and L. N. Sankar. Ground effect of a rotor hovering above a confined area. *Frontiers in Aerospace Engineering*, 3(1), 2014.

[3] M. F. Konuş and Ö. Savaş. Rotor vortex wake in close proximity of walls in hover. *Journal of the American Helicopter Society*, 61(4):1–12, 2016.

[4] D. Lee, N. Sezer-Uzol, J. F. Horn, and L. N. Long. Simulation of helicopter shipboard launch and recovery with time-accurate airwakes. *Journal of Aircraft*, 42(2):448–461, 2005.

[5] R. G. Lee and S. J. Zan. Unsteady aerodynamic loading on a helicopter fuselage in a ship airwake. *Journal of the American Helicopter Society*, 49(2):149–159, 2004.

[6] R. G. Lee and S. J. Zan. Wind tunnel testing of a helicopter fuselage and rotor in a ship airwake. *Journal of the American Helicopter Society*, 50(4):326–337, 2005.

[7] Y. Nacakli and D. Landman. Helicopter downwash/frigate airwake interaction flowfield piv surveys in a low speed wind tunnel. In *AHS 67th annual forum*, pages 1–11, 2011.

[8] T. Quinliven and K. Long. Rotor performance in the wake of a large structure. In *American Helicopter Society 65th Annual Forum*, May 2009.

[9] G. Rajagopalan, S. Niazi, A. Wadcock, G.K.Yamauchi, and M. Silva. Experimental and computational study of the interaction between a tandem-rotor helicopter and a ship. In *American Helicopter Society* 61^{th} *Annual Forum*, June 1-3 2005.

[10] G. K. Timm. Obstacleinduced flow recirculation. *Journal of the American Helicopter Society*, 10(4):5–24, 1965.

[11] U.S. Joint Helicopter Safety Analysis Team. The compendium report:the u.s. jhsat baseline of helicopter accident analysis. Technical report, International Helicopter Safety Team, 2011.

[12] S. Zan. Experimental determination of rotor thrust in a ship airwake. *Journal of the American Helicopter Society*, 47(2):100–108, 2002.

[13] S. Zan. On aerodynamic modelling and simulation of the dynamic interface. *Proceedings of the Institution of Mechanical Engineers, Part G: Journal of Aerospace Engineering*, 219(5):393–410, 2005.

Figures

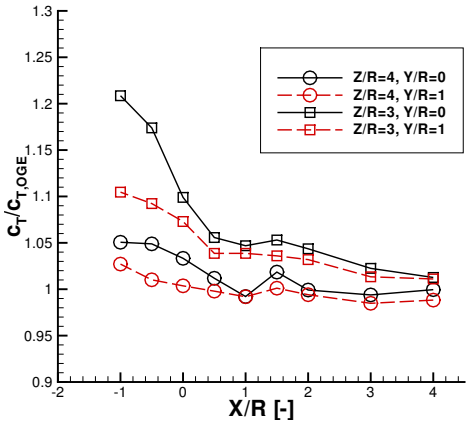

(a) Ratio between the Thrust Coefficient c_T and the one measured in OGE, $Z/R = 3, 4$

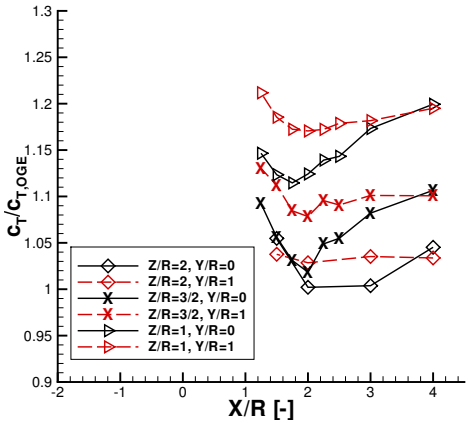

(b) Ratio between the Thrust Coefficient c_T and the one measured in OGE, $Z/R = 1, 3/2, 2$

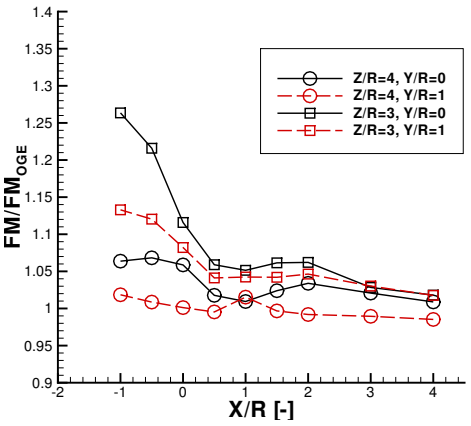

(c) Ratio between the Figure of Merit and the one measured in OGE, $Z/R = 3, 4$

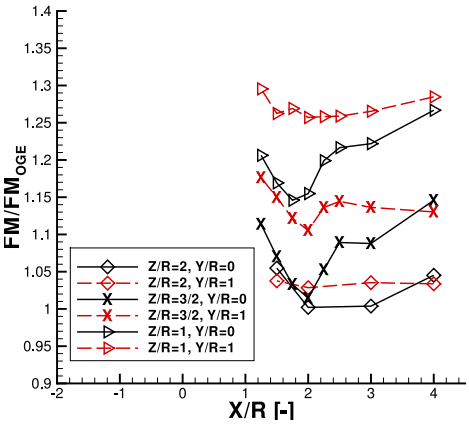

(d) Ratio between the Figure of Merit and the one measured in OGE, $Z/R = 1, 3/2, 2$

Figure 6: Thrust coefficient and Figure of Merit vs rotor position, at different rotor heights

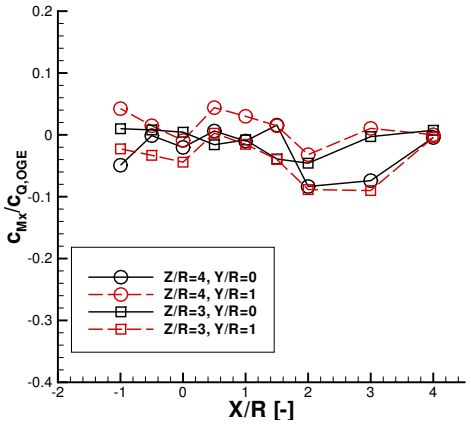

(a) Ratio between $x-$moment coeff. and the OGE torque coeff., $Z/R = 3, 4$

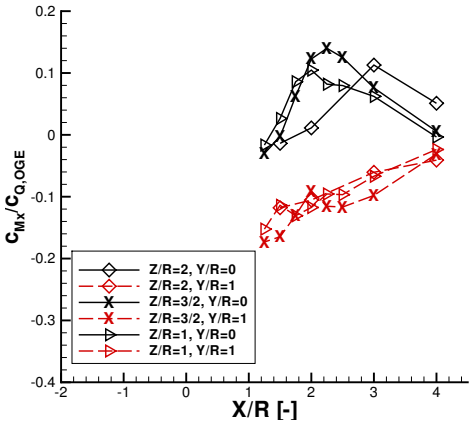

(b) Ratio between $x-$moment coeff. and the OGE torque coeff., $Z/R = 1, 3/2, 2$

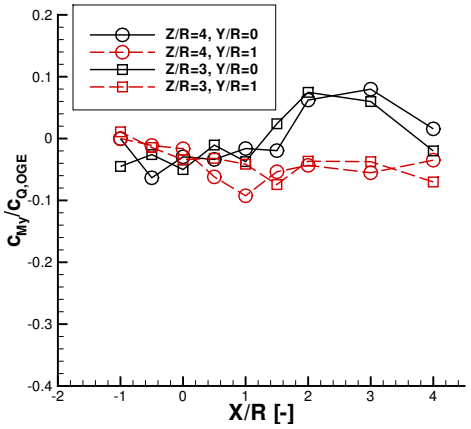

(c) Ratio between $x-$moment coeff. and the OGE torque coeff., $Z/R = 3, 4$

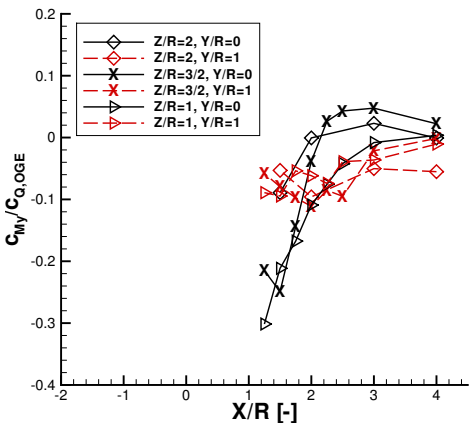

(d) Ratio between $x-$ moment coeff. and the OGE torque coeff., $Z/R = 1, 3/2, 2$

Figure 7: x and y moment coefficients vs rotor position, at different rotor heights

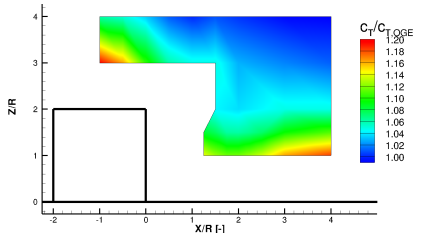

(a) Ratio between the Thrust Coefficient c_T and the one measured in OGE, $Y/R = 0$

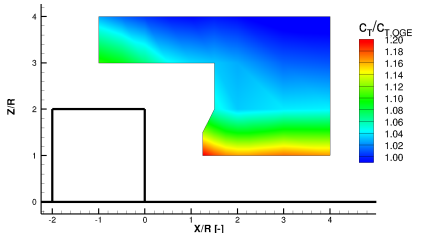

(b) Ratio between the Thrust Coefficient c_T and the one measured in OGE, $Y/R = 1$

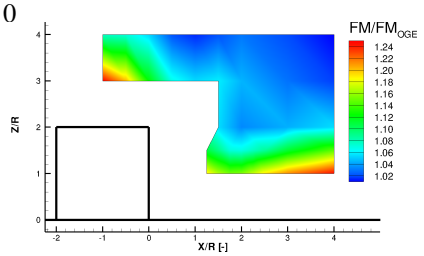

(c) Ratio between the Figure of Merit and the one measured in OGE. $Y/R = 0$

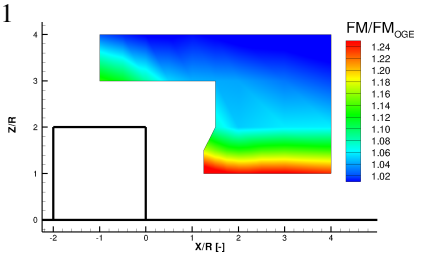

(d) Ratio between the Figure of Merit and the one measured in OGE. $Y/R = 1$

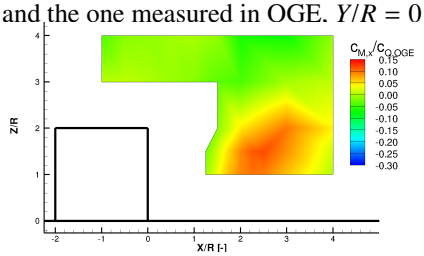

(e) Ratio between $x-$moment coeff. and the OGE torque coeff., $Y/R = 0$

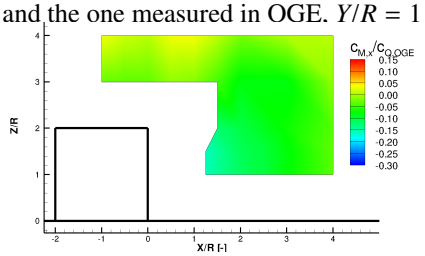

(f) Ratio between $x-$moment coeff. and the OGE torque coeff., $Y/R = 1$

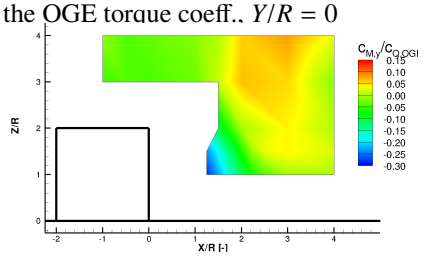

(g) Ratio between $y-$moment coeff. and the OGE torque coeff., $Y/R = 0$

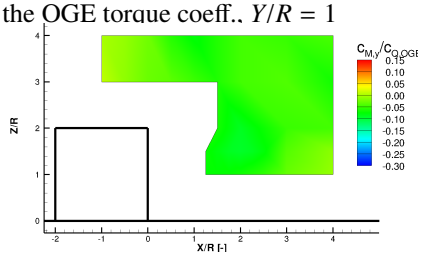

(h) Ratio between $y-$moment coeff. and the OGE torque coeff., $Y/R = 1$

Figure 8: Contours of the loads acting on the rotor vs rotor position. Rotor placed at $Y/R = 0$, left, and at $Y/R = 1$, right.

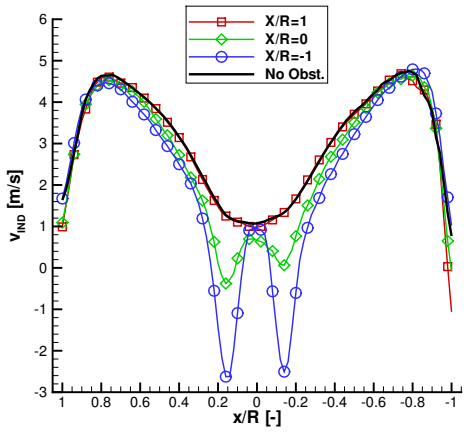

(a) $Z/R = 3$, $Y/R = 0$

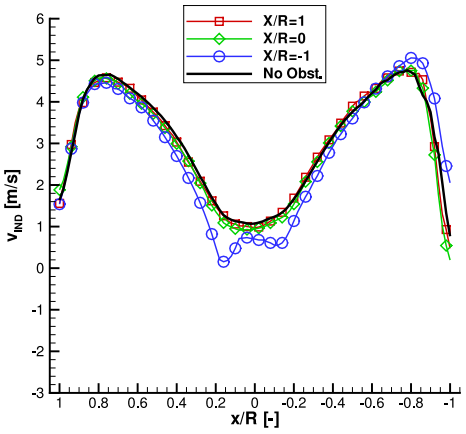

(b) $Z/R = 3$, $Y/R = 1$

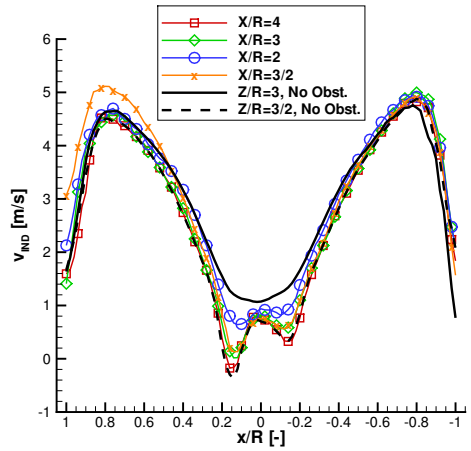

(c) $Z/R = 3/2$, $Y/R = 0$. The obstacle is on the left of the plot.

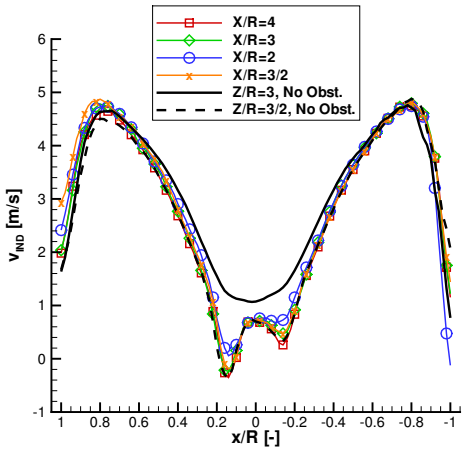

(d) $Z/R = 3/2$, $Y/R = 1$. The obstacle is on the left of the plot.

Figure 9: LDA Measurement of the induced velocity, x-sweep. Rotor placed at $Y/R = 0$, left, and at $Y/R = 1$, right.

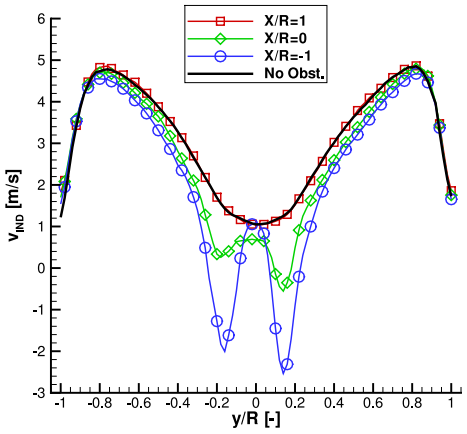

(a) $Z/R = 3$, $Y/R = 0$

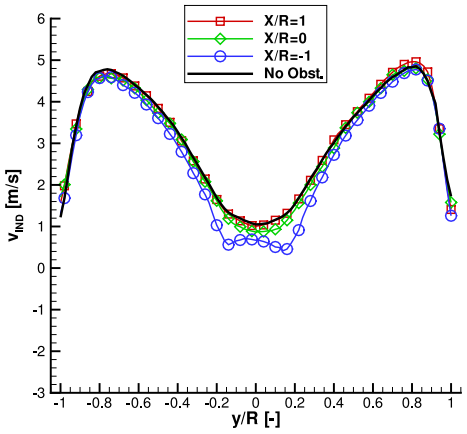

(b) $Z/R = 3$, $Y/R = 1$

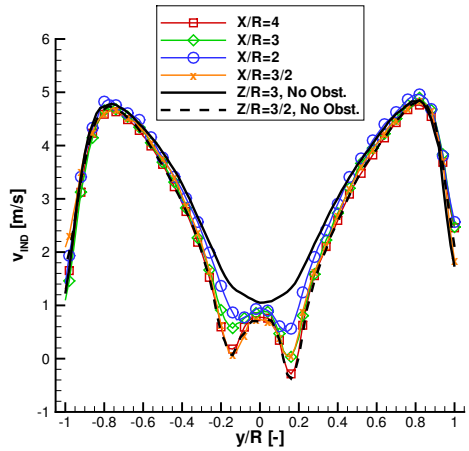

(c) $Z/R = 3/2$, $Y/R = 0$. The obstacle is on the left of the plot.

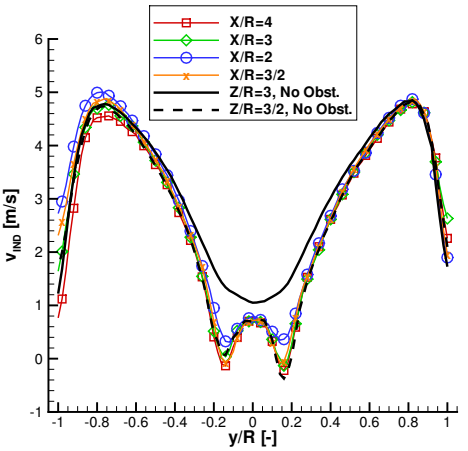

(d) $Z/R = 3/2$, $Y/R = 1$. The obstacle is on the left of the plot.

Figure 10: LDA Measurement of the induced velocity, y-sweep. Rotor placed at $Y/R = 0$, left, and at $Y/R = 1$, right.

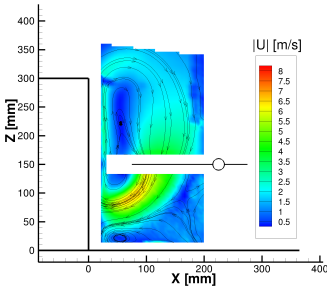

(a) X/R=3/2, Y/R=0, Z/R=1

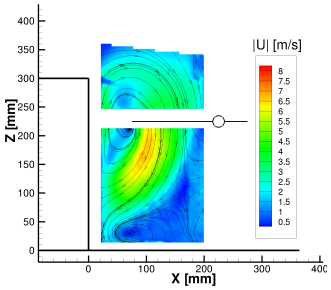

(b) X/R=3/2, Y/R=0, Z/R=3/2

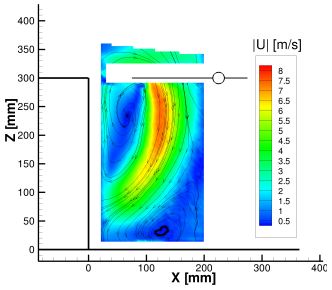

(c) X/R=3/2, Y/R=0, Z/R=2

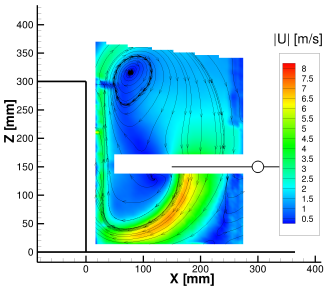

(d) X/R=2, Y/R=0, Z/R=1

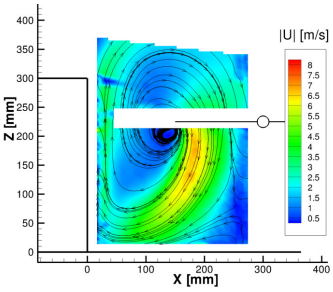

(e) X/R=2, Y/R=0, Z/R=3/2

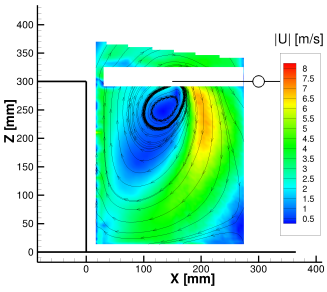

(f) X/R=2, Y/R=0, Z/R=2

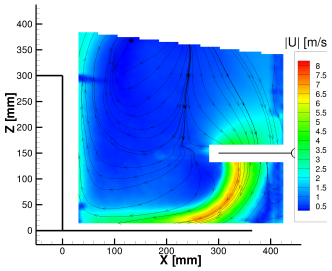

(g) X/R=3, Y/R=0, Z/R=1

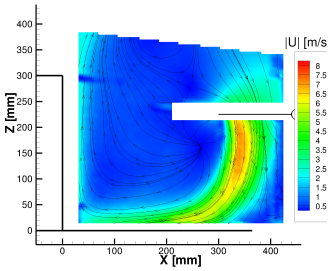

(h) X/R=3, Y/R=0, Z/R=3/2

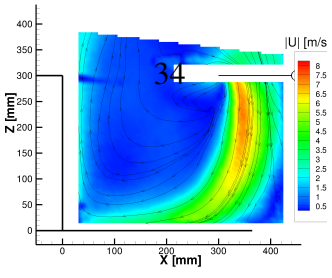

(i) X/R=3, Y/R=0, Z/R=2

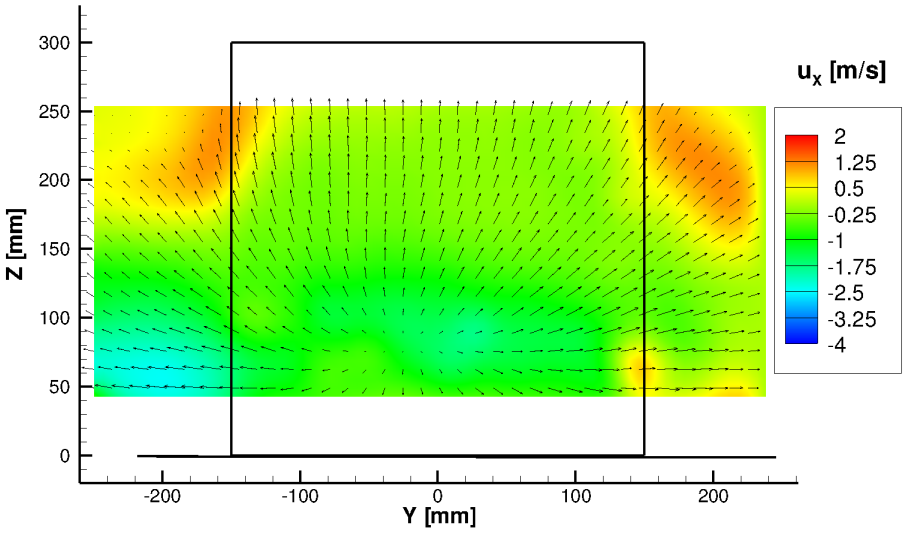

(a) Transverse measurement plane at $X/R = 0.1$

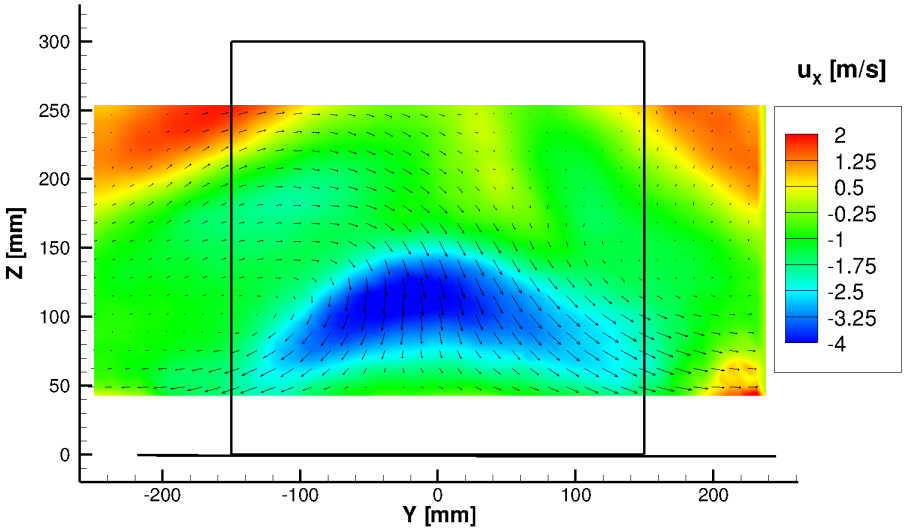

(b) Transverse measurement plane at $X/R = 0.466$

Figure 12: Out-of-plane velocity contours and in-plane velocity vectors. Rotor Placed at $X/R = 3/2$, $Y/R = 0$, $Z/R = 2$. A negative out-of-plane velocity points towards the obstacle

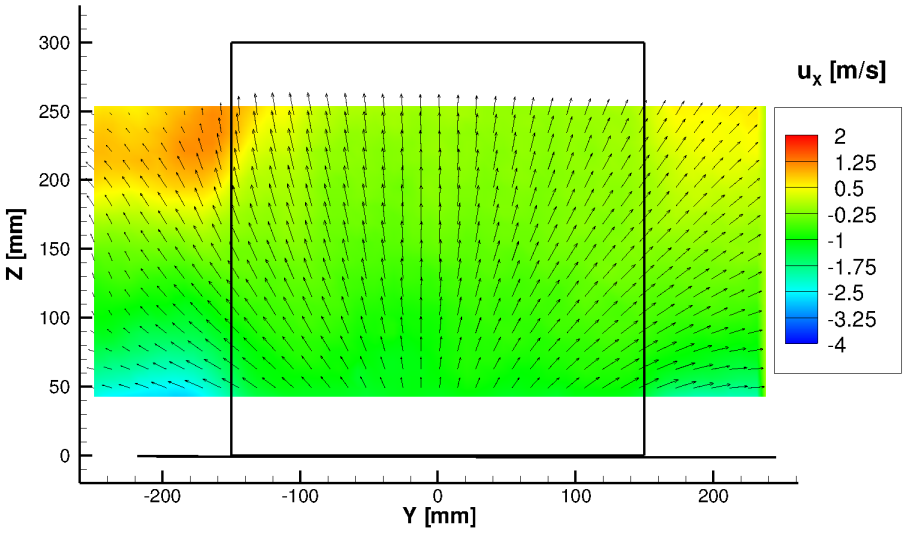

(a) Transverse measurement plane at $X/R = 0.1$

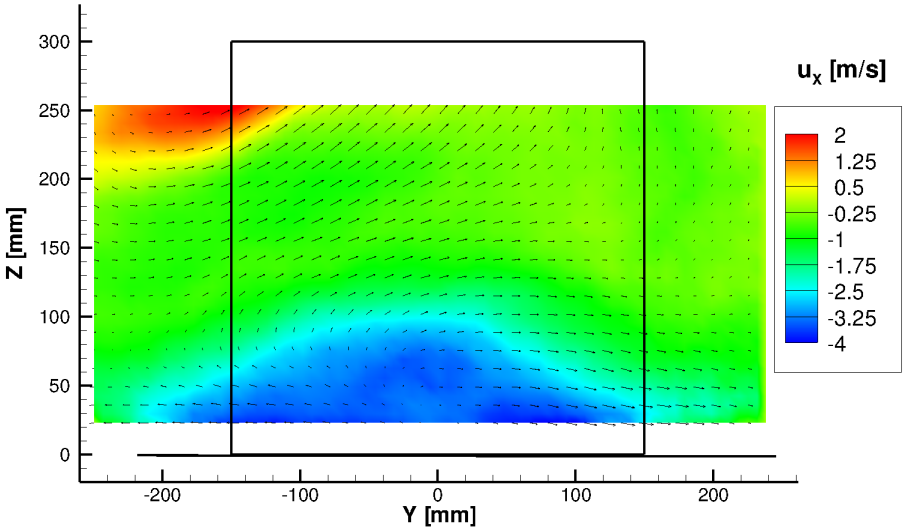

(b) Transverse measurement plane at $X/R = 0.466$

Figure 13: Out-of-plane velocity contours and in-plane velocity vectors. Rotor Placed at $X/R = 2$, $Y/R = 0$, $Z/R = 2$. A negative out-of-plane velocity points towards the obstacle

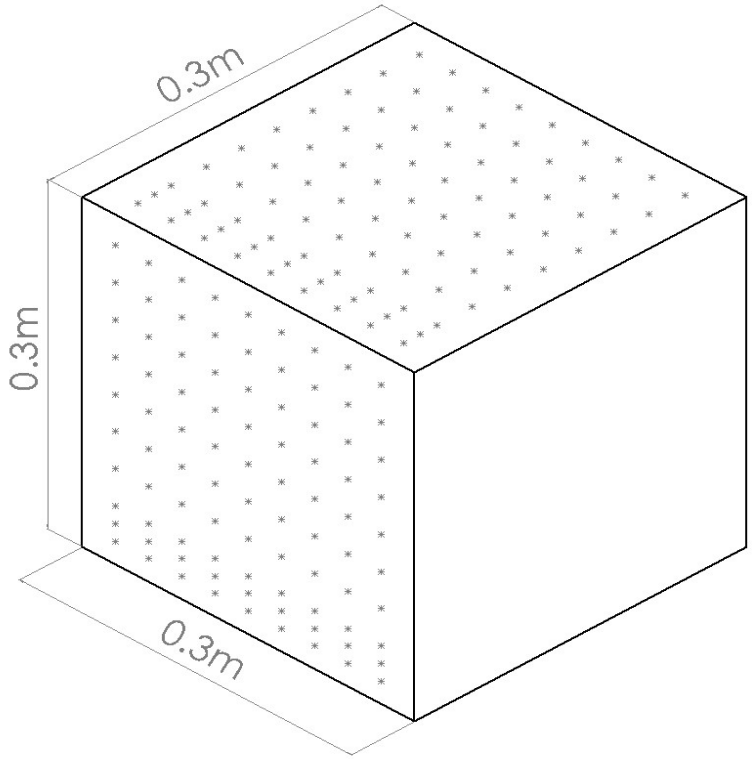

Figure 14: Schematic diagram of the obstacle and the locations of the pressure tappings.

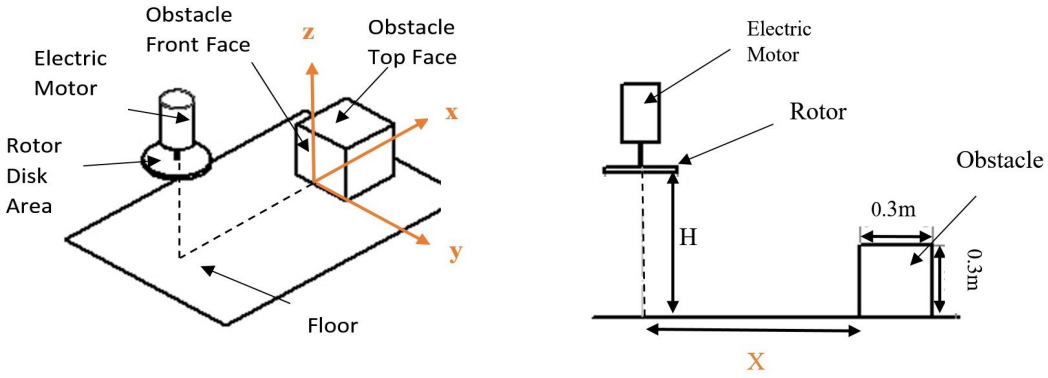

Figure 15: Pressure tapping experimental rig configuration and axis definitions. H is the height of the rotor above the ground, equivalent to Z.

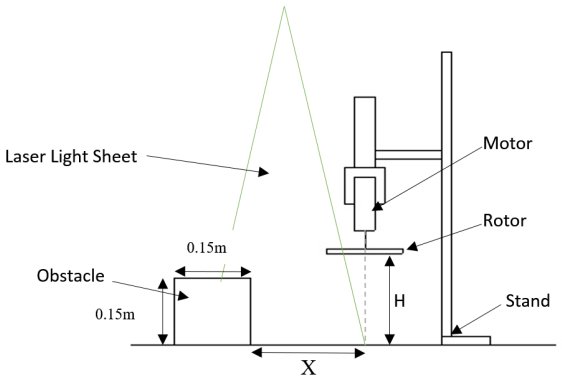

Figure 16: Schematic diagram of the experimental rig used for the additional PIV experiments. H is the height of the rotor above the ground, equivalent to Z.

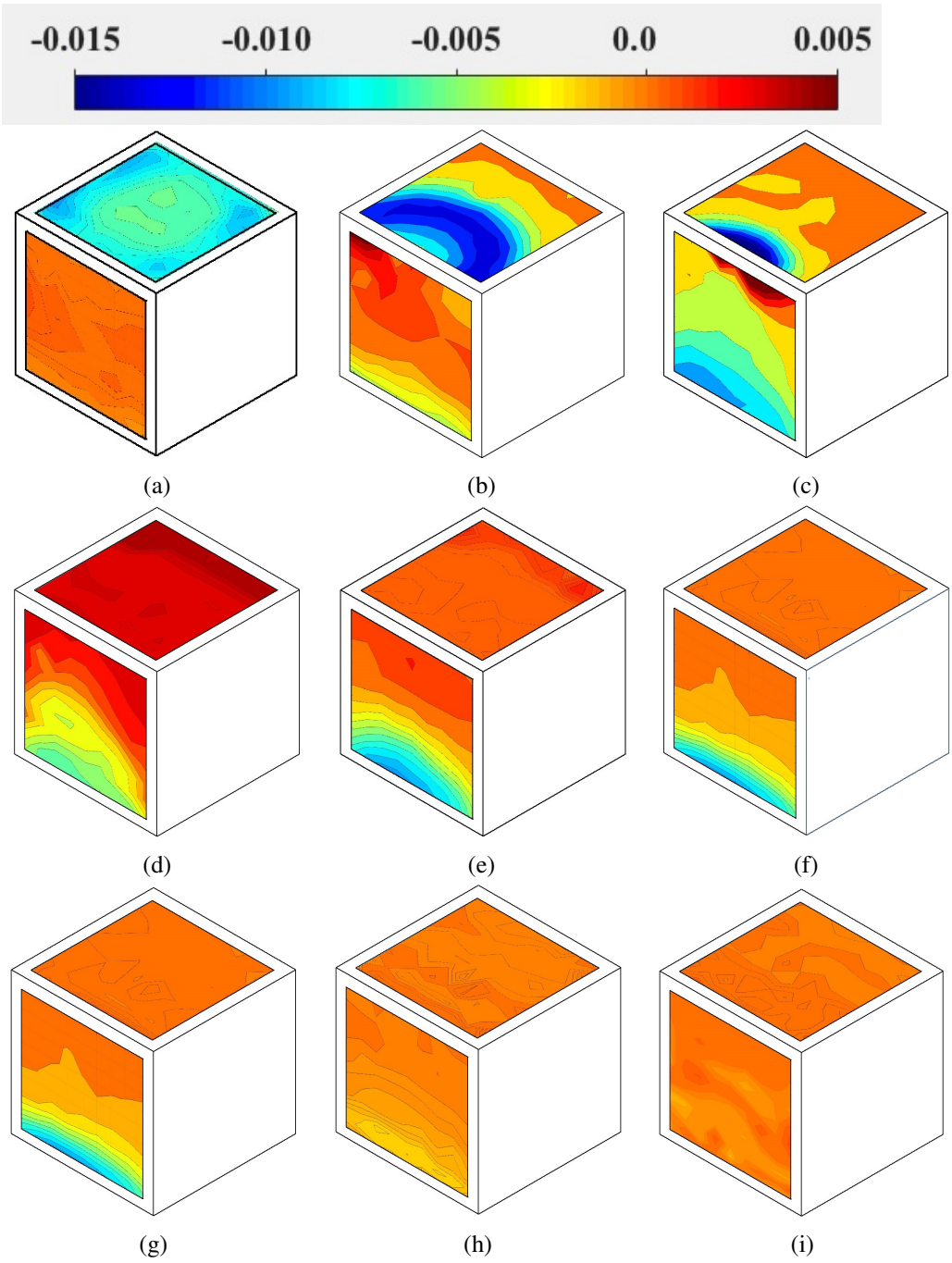

Figure 17: Surface plots of (-C_p) on the obstacle front and top faces with the rotor at $\frac{Z}{R}$ = 3.86 and the obstacle at: ((a) $\frac{X}{R} = -1$, (b) $\frac{X}{R}$ = 0, (c) $\frac{X}{R}$ = 0.5, (d) $\frac{X}{R}$ = 1, (e) $\frac{X}{R}$ = 1.5, (f) $\frac{X}{R}$ = 2.0, (g) $\frac{X}{R}$ = 4.0, (h) $\frac{X}{R}$ = 6.0 (i) $\frac{X}{R}$ = 8.0

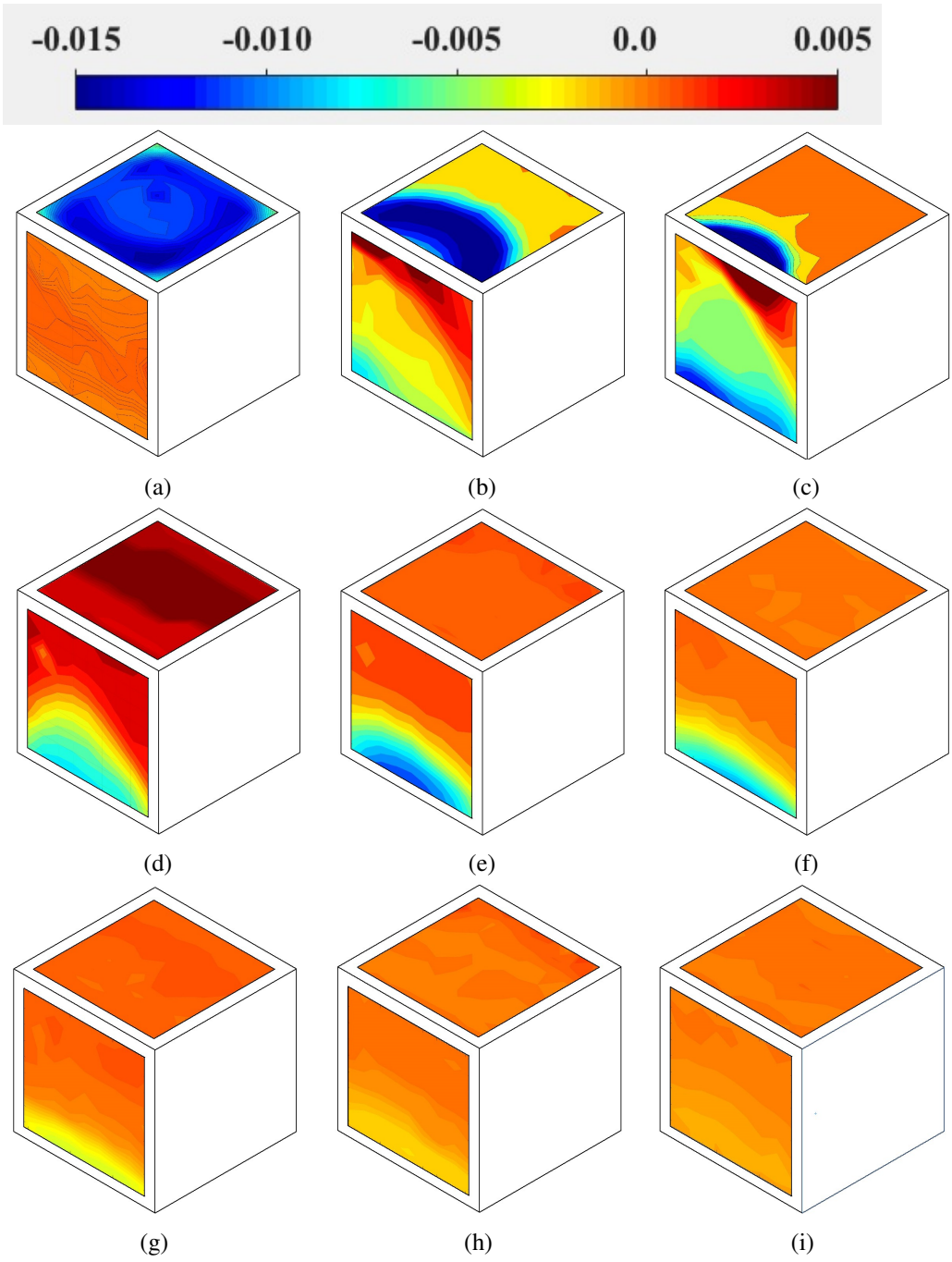

Figure 18: Surface plots of (-C_p) on the obstacle front and top faces with the rotor at $\frac{Z}{R} = 2.86$ and the obstacle at: (a) $\frac{X}{R} = -1$, (b) $\frac{X}{R} = 0$, (c) $\frac{X}{R} = 0.5$, (d) $\frac{X}{R} = 1$, (e) $\frac{X}{R} = 1.5$, (f) $\frac{X}{R} = 2.0$, (g) $\frac{X}{R} = 4.0$, (h) $\frac{X}{R} = 6.0$ (i) $\frac{X}{R} = 8.0$

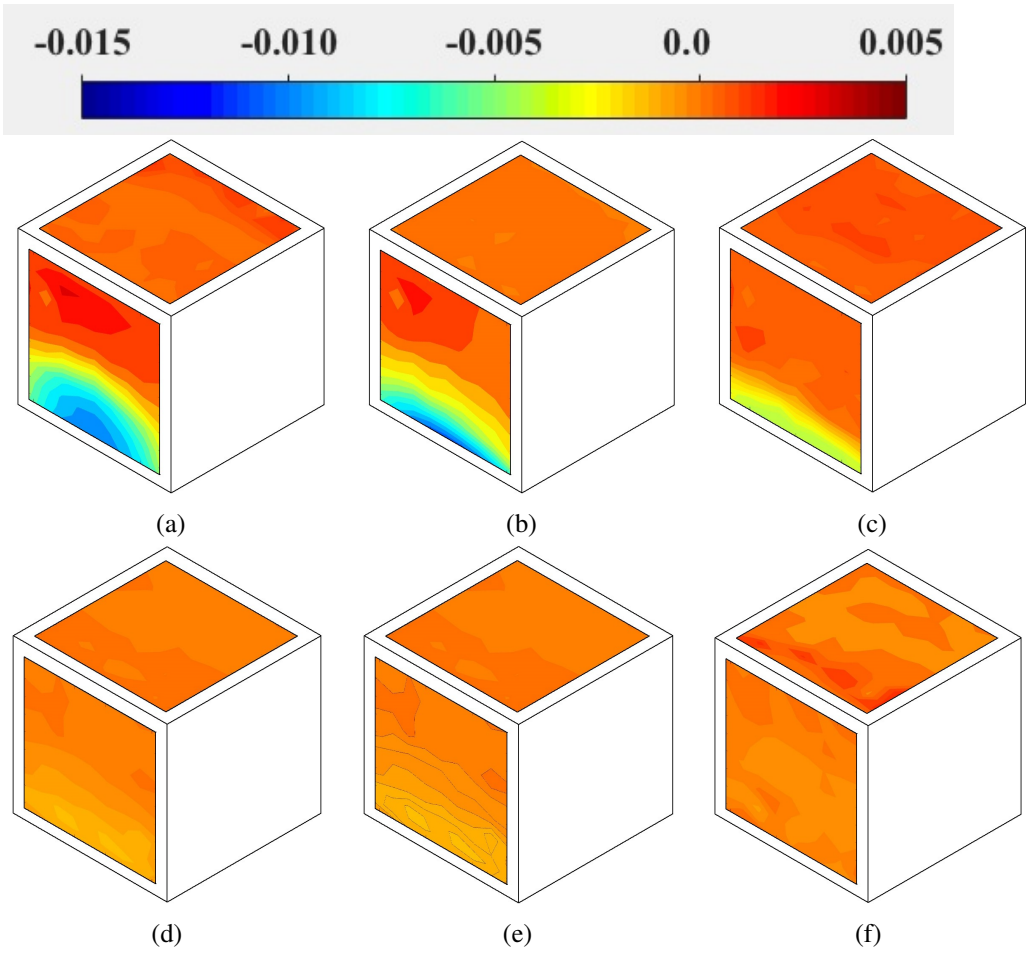

Figure 19: Surface plots of (-C_p) on the obstacle front and top faces with the rotor at $\frac{Z}{R}$ = 2.0 and the obstacle at: (a) $\frac{X}{R}$ = 1.5, (b) $\frac{X}{R}$ = 2.0, (c) $\frac{X}{R}$ = 4.0, (d) $\frac{X}{R}$ = 6.0 (e) $\frac{X}{R}$ = 7, (f) $\frac{X}{R}$ = 8.0.

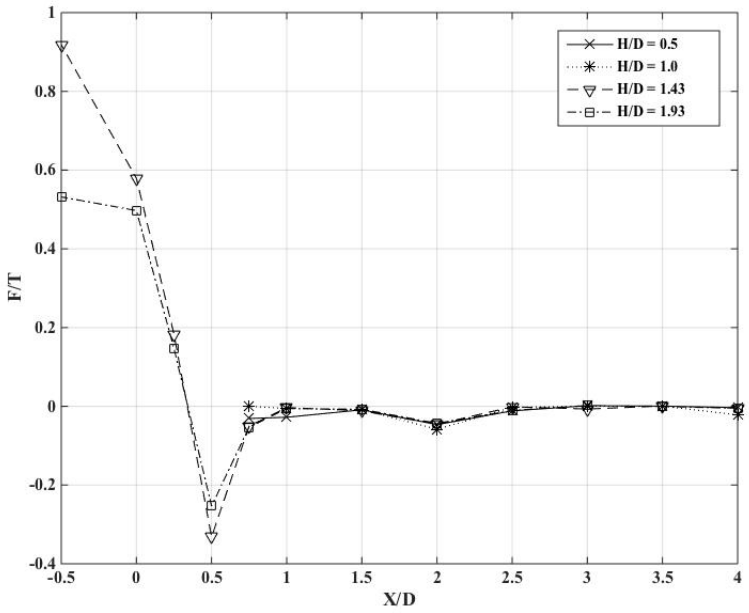

Figure 20: Variation of the non-dimensional force $\frac{F}{T}$ experienced by the top face of the obstacle as the lateral displacement $\frac{X}{D}$ between the rotor axis and the obstacle front face varied. Note horizontal axis shows X/D and not X/R.

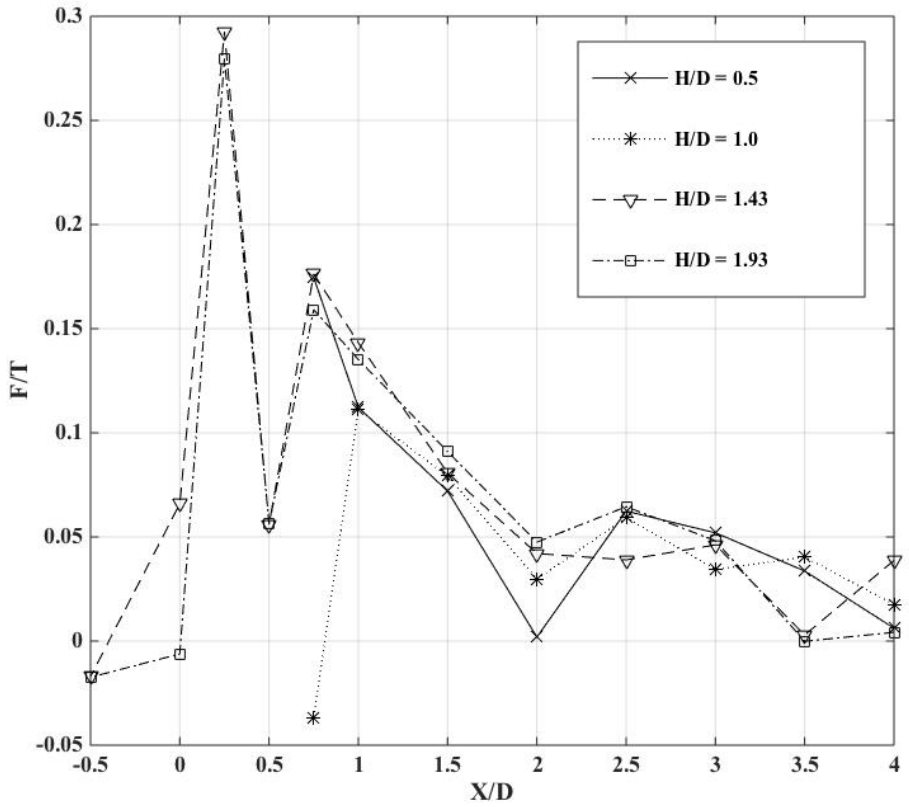

Figure 21: Variation of the non-dimensional force $\frac{F}{T}$ experienced by the front face of the obstacle as the lateral displacement $\frac{X}{D}$ between the rotor axis and the obstacle front face varied. Note horizontal axis shows X/D and not X/R.

(a) rotor at X/R = -1

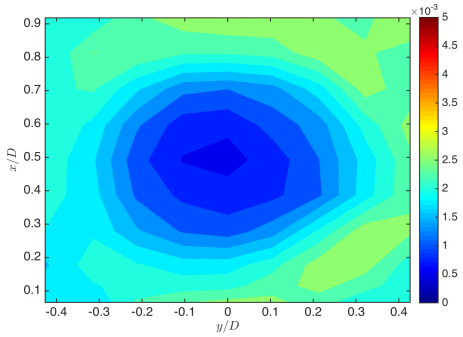

(b) rotor at X/R = 0

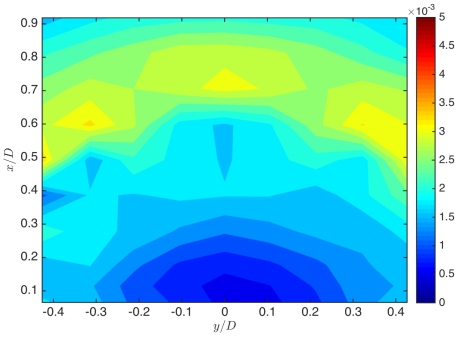

(c) rotor at X/R = 0.5

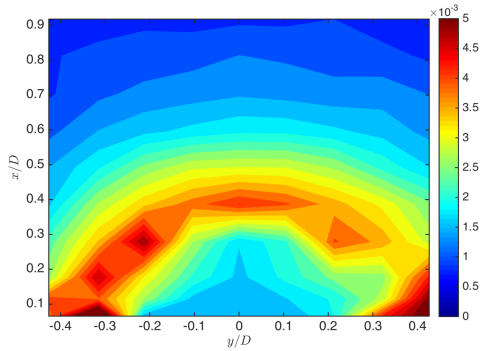

Figure 22: Contour plots of the RMS pressure variation on the obstacle top face with rotor height at $\frac{Z}{R}$ =2.86 and obstacle at (a) $\frac{X}{R} = -1$, (b) $\frac{X}{R} = 0$, (c) $\frac{X}{R} = 0.5$

(a) rotor at $Z/R = 2.86$

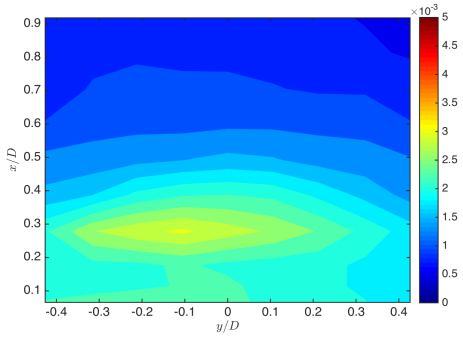

(b) rotor at $Z/R = 2.0$

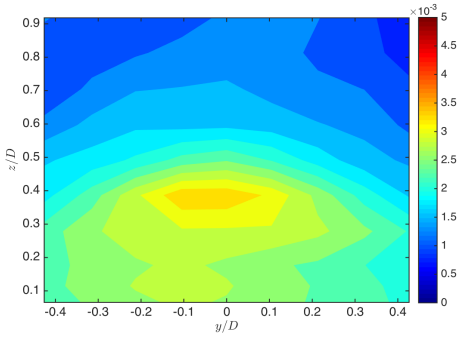

(c) rotor at $Z/R = 1.0$

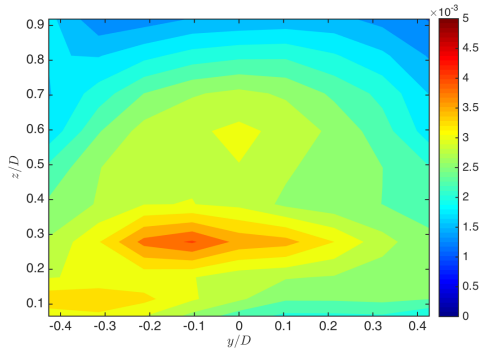

Figure 23: Contour plots of the RMS pressure variation on the obstacle front face with rotor spacing at $\frac{X}{R}$ =1.5and rotor at (a) $\frac{Z}{R} = 2.86$, (b) $\frac{Z}{R} = 2.0$, (c) $\frac{Z}{R} = 1.0$

(a) tapping at $x/D = 0.38$

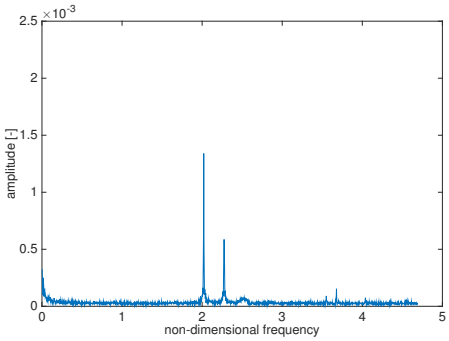

(b) tapping at $x/D = 0.70$

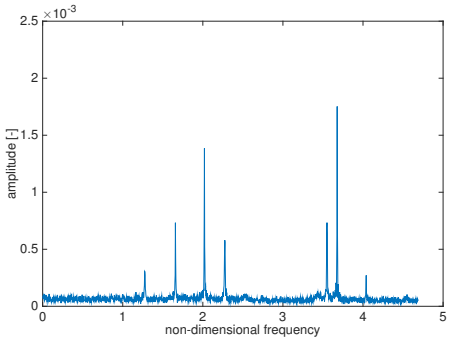

(c) tapping at x/D =0.92

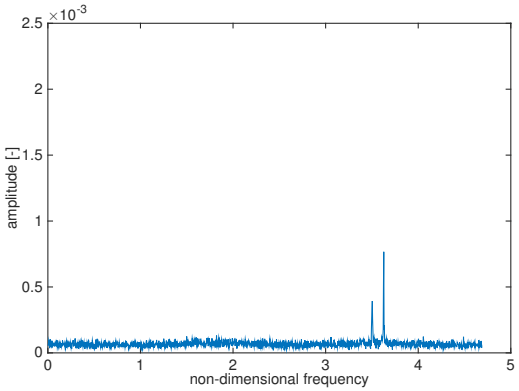

Figure 24: Frequency spectra of individual pressure tapping signals along the centre-line of the obstacle top surface for rotor height Z/R =2.86, obstacle spacing X/R =0. Frequency has been scaled with the rotor rotational frequency, amplitude has been scaled with $\frac{1}{2}\rho V_{TIP}^2$.

(a) tapping at $x/D = 0.17$

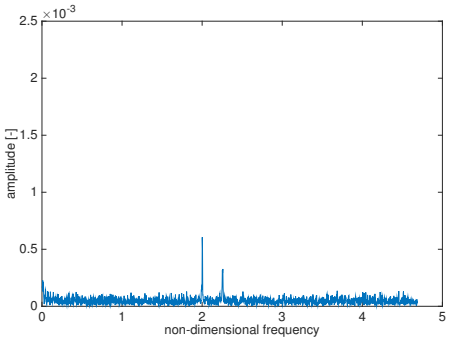

(b) tapping at $x/D = 0.38$

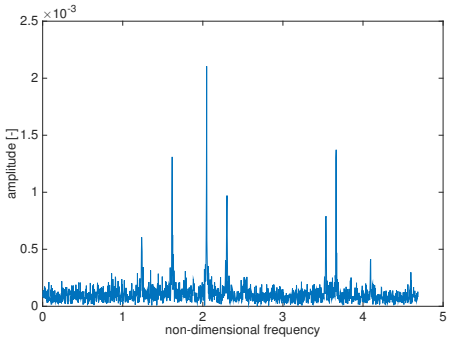

(c) tapping at x/D =0.70

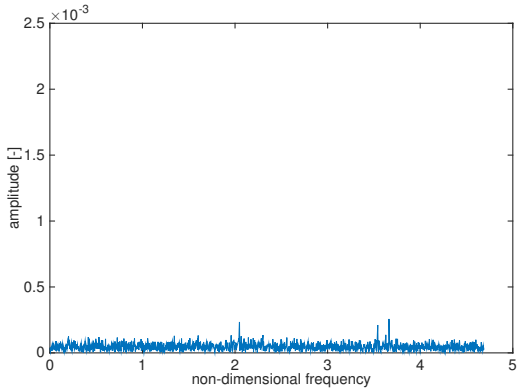

Figure 25: Frequency spectra of individual pressure tapping signals along the centre-line of the obstacle top surface for rotor height Z/R =2.86, obstacle spacing X/R =0.5. Frequency has been scaled with the rotor rotational frequency, amplitude has been scaled with $\frac{1}{2}\rho V_{TIP}^2$.

(a) no obstacle

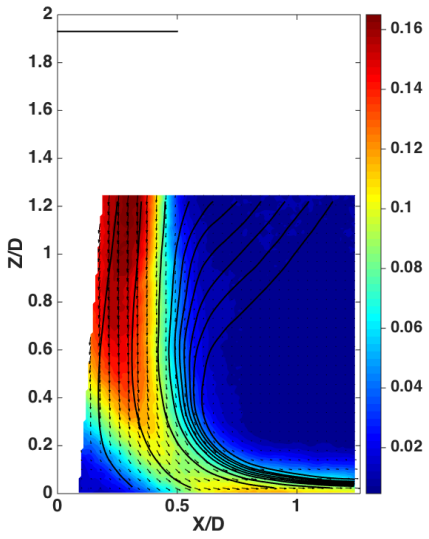

(b) obstacle at X/D=-0.5

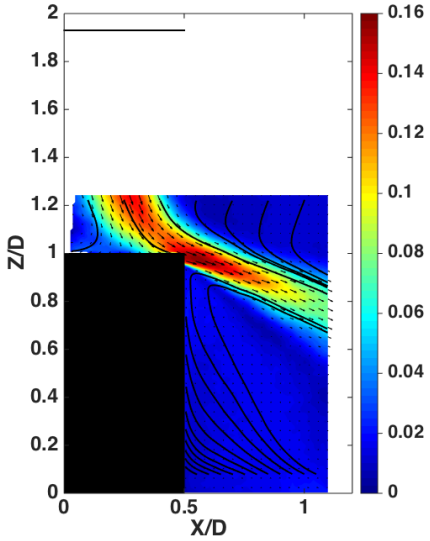

(c) obstacle at X/D=1.0

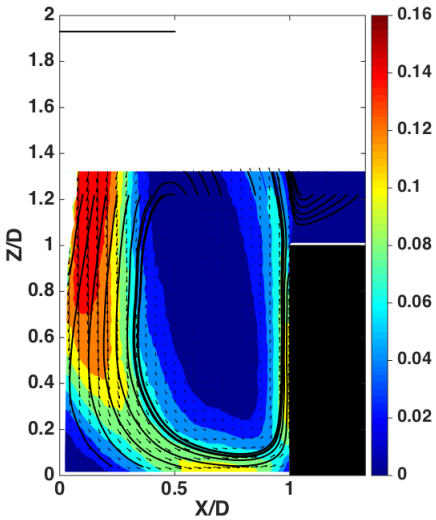

Figure 26: Contour plot of the PIV mean flow velocities produced with the rotor at $\frac{Z}{R} = 3.86$ with (a) no obstacle, (b) obstacle at X/D=-0.5, (c) obstacle at X/D=1.0. The contours are in-plane velocity magnitude scaled with respect to rotor tip velocity. Note that the axes are scaled with respect to rotor diameter D.

(a) obstacle at X/D=-0.5

(b) obstacle at X/D=0.5

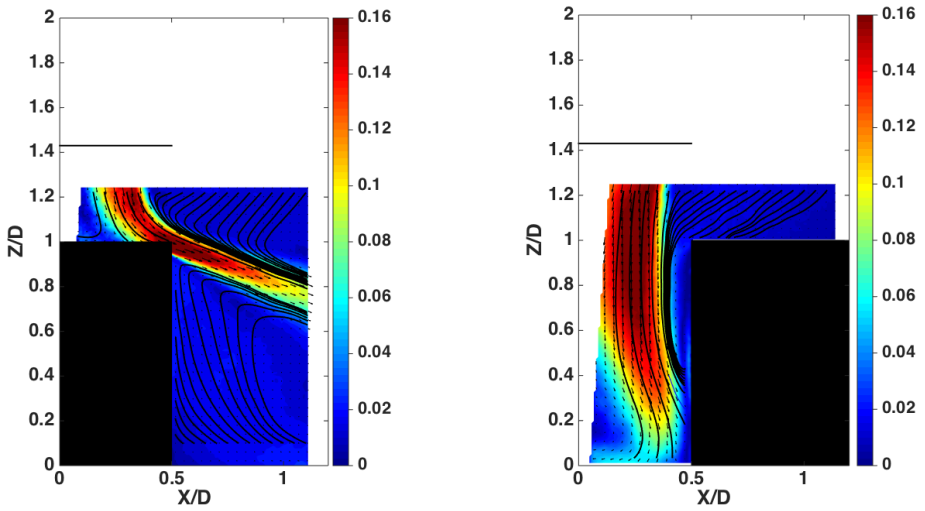

Figure 27: Contour plot of the PIV mean flow velocities produced with the rotor at $\frac{Z}{R} = 2.86$ with the obstacle at (a) obstacle at X/D=-0.5, (b) obstacle at X/D=0.5. The contours are in-plane velocity magnitude scaled with respect to rotor tip velocity. Note that the axes are scaled with respect to rotor diameter D.

(a) no obstacle (b) obstacle at X/D=1.0

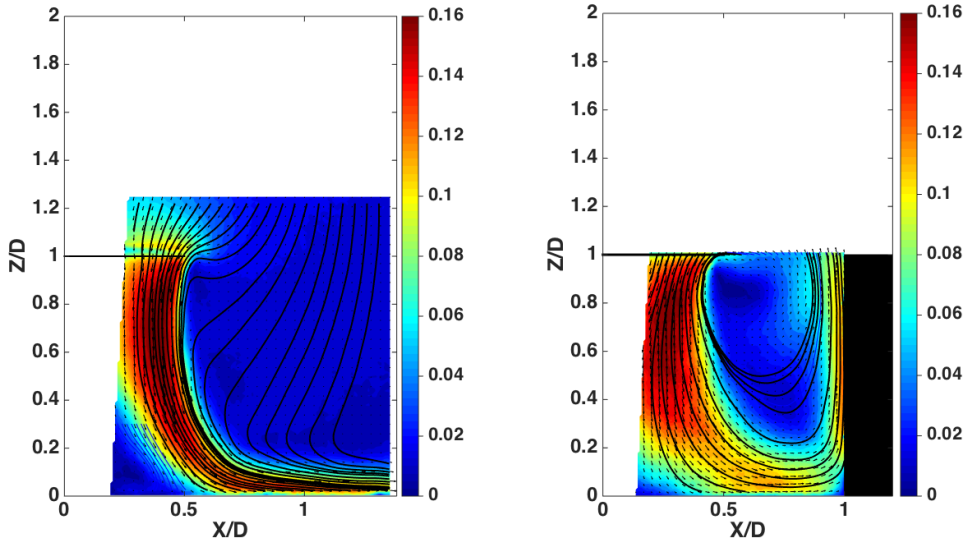

Figure 28: Contour plot of the PIV mean flow velocities produced with the rotor at $\frac{Z}{R} = 2.0$ (a) without the obstacle, (b) wth the obstacle at X/D=1.0. The contours are in-plane velocity magnitude scaled with respect to rotor tip velocity. Note that the axes are scaled with respect to rotor diameter D.

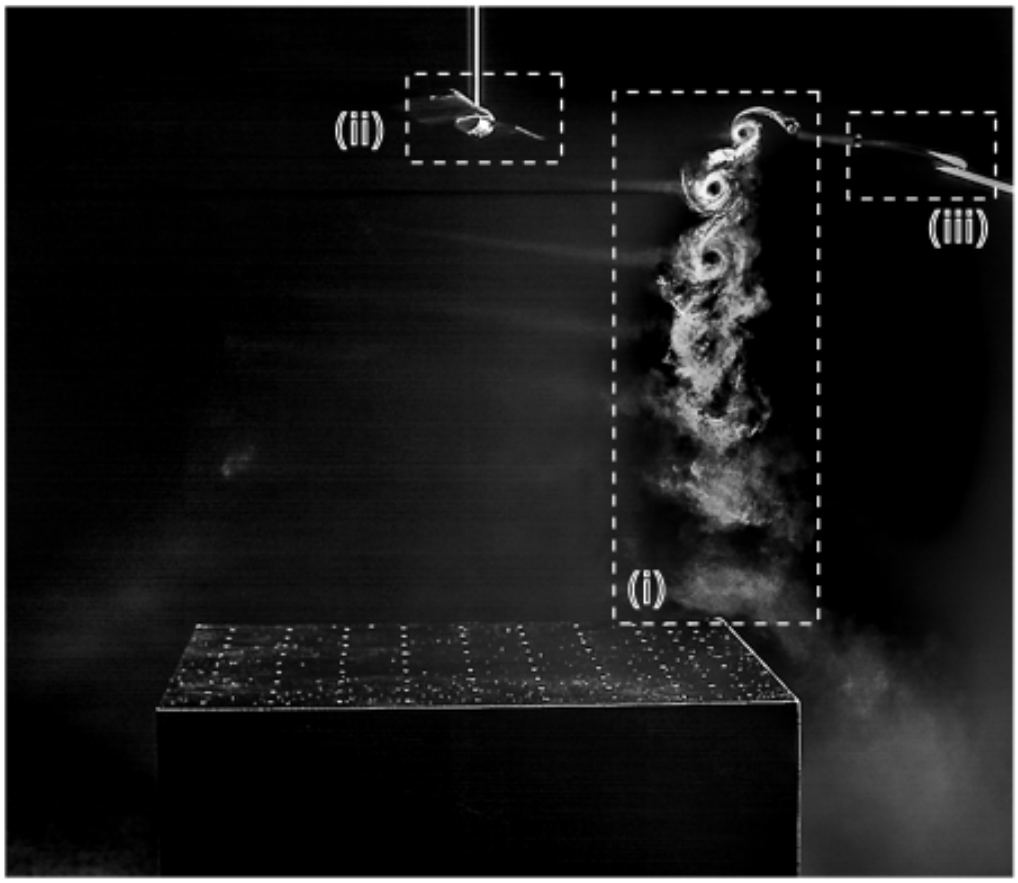

Figure 29: Smoke flow image of the rotor wake produced with the rotor at $\frac{Z}{R} = 3.86$ and the obstacle at $\frac{X}{R} = -1$. (i) Blade Tip Vortices (ii) Rotor (iii) Smoke Wand

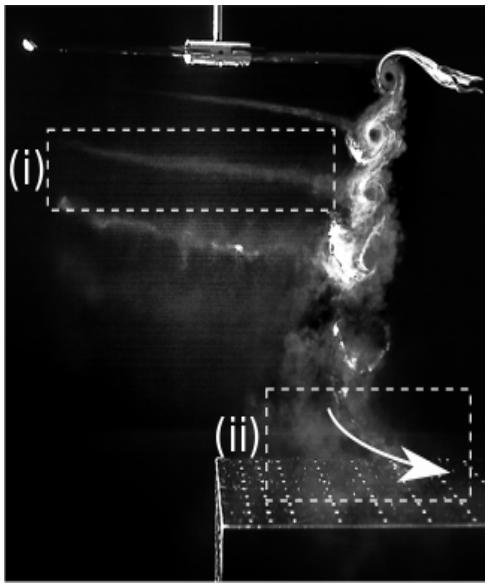

Figure 30: Smoke flow images of the rotor wake produced with the rotor at $\frac{Z}{R} = 3.86$ and the obstacle at $\frac{X}{R} = 0.0$. (i) part of helical vortex filament, (ii) vortices impacting on upper surface of obstacle

Figure 31: Smoke flow image of the rotor wake with the rotor at $\frac{Z}{R} = 3.86$ and the obstacle at $\frac{X}{R} = 1$. Smoke entrained into the vortices passing down past the front face of the obstacle.

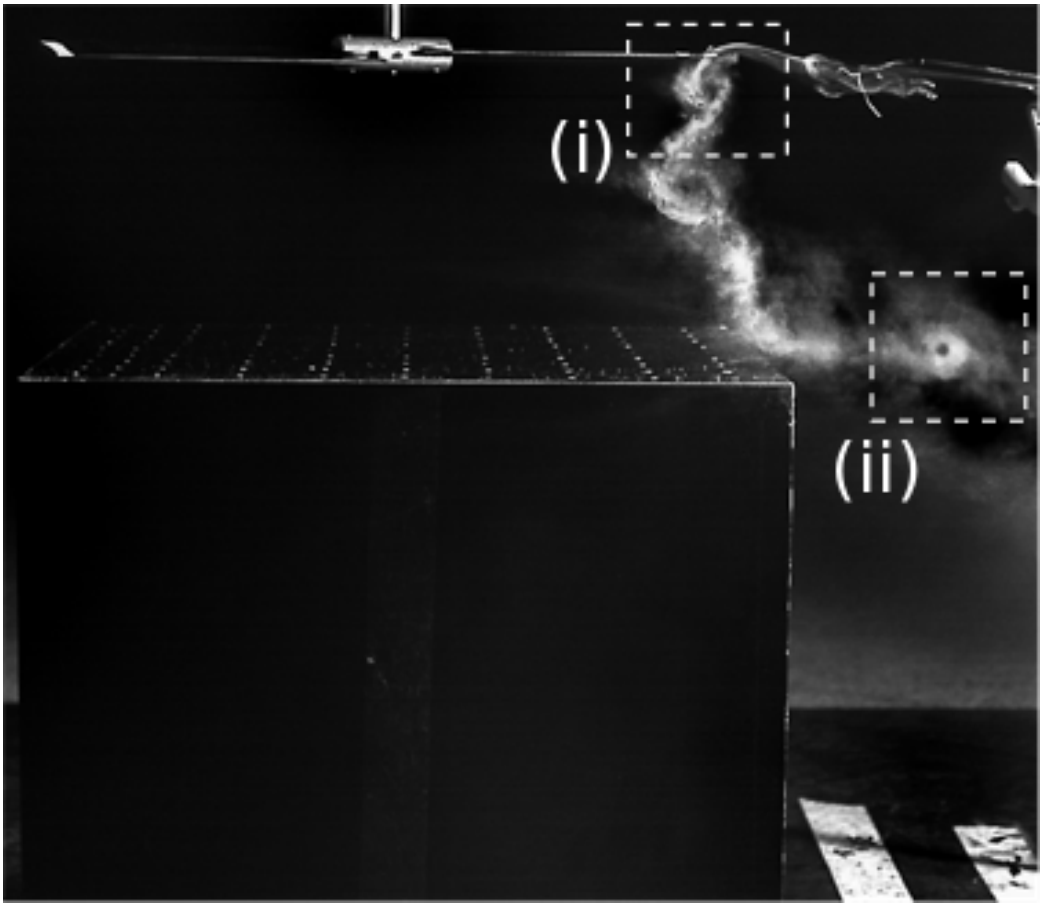

Figure 32: Smoke flow image of the rotor wake produced with the rotor at $\frac{Z}{R} = 2.86$ and the obstacle at $\frac{X}{R} = -1$. (i) Blade tip vortex (ii) Deflected blade tip vortex

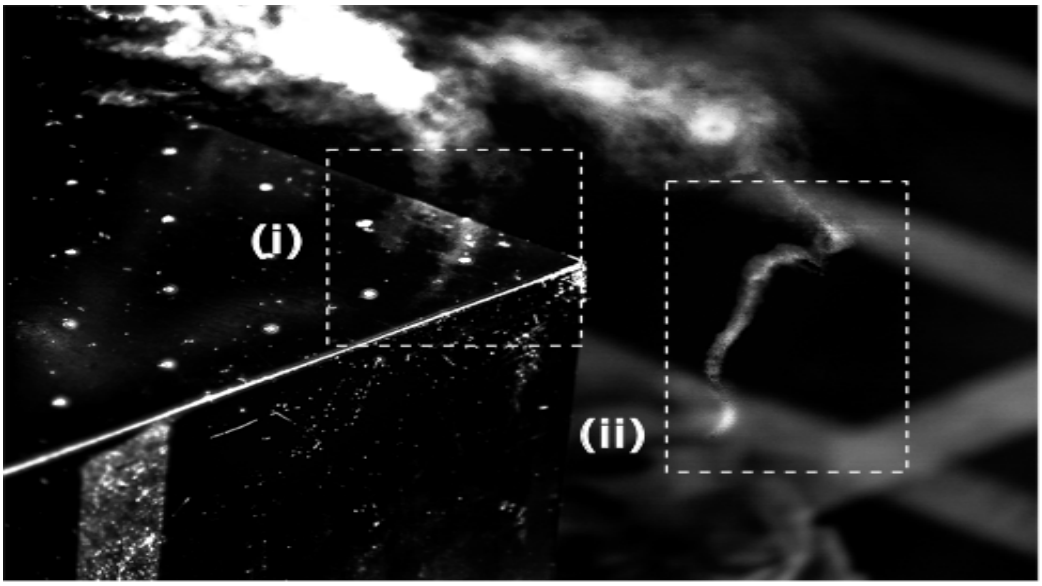

Figure 33: Smoke flow image of the deformation of the blade tip vortex interactions with the obstacle produced with the rotor operating at $\frac{Z}{R} = 2.86$ and the obstacle located at $\frac{X}{R} = -1$.(i) Vortex filament prior to passing over corner (ii) Deformed segment of vortex filament after passing over corner.